A Bayesian Approach to 2D Acceleration for Studying Activation Detection Rate for Simultaneously Encoded Slice Acquisition in FMRI

Ke Xu[a], Daniel B. Rowe[a,*]

[a] *Computational Mathematical and Statistical Sciences, Marquette University, 1313 W Wisconsin Ave, Milwaukee, 53233, WI, USA*

Abstract

Functional Magnetic Resonance Imaging (fMRI) enables researchers to study brain functions and advance understanding in human sciences. Spatial and temporal changes in brain metabolism as by detecting the Blood Oxygen Level Dependent (BOLD) contrast signal are represented in the frequency domain of an image, known as k-space. Traditional MRI methodologies require full k-space information, which follows a unique data acquisition sequence to reconstruct the complete image. This process presents a time-consuming obstacle for medical imaging techniques. Our study proposes a novel image reconstruction method to enhance the efficiency of data acquisition while maintaining high accuracy in activation detection. The through-plane and in-plane acceleration techniques are combined to accelerate image acquisition along two dimensions. Multiple image-shift strategies and a 2D Hadamard encoding scheme are used to increase encoding diversity and reduce slice leakage. By applying our approach to both simulated and experimental fMRI data, we successfully reduced total scan time while achieving a higher signal-to-noise ratio (SNR) and contrast-to-noise ratio (CNR) in regions of interest (ROI). Compared with conventional reconstruction strategies, the proposed method demonstrates potential improvements in activation detection under specific acceleration and encoding conditions, while also providing voxel-wise estimates through a Bayesian framework.

Keywords:

---

[*] Corresponding author.

Email address: `daniel.rowe@marquette.edu` (Daniel B. Rowe)

fMRI, SMS, 2D Acceleration, CAIPI-VAT, Bayesian

---

1. Introduction

1.1. *Complex-Valued Bayesian Model*

Functional magnetic resonance imaging (fMRI) studies can be interpreted following the Bayesian methodology but with complex-valued observations. To set up a complex-valued Bayesian linear model, the complex-valued observation can be written as Eq. 1:

$$a_C = X_C \beta_C + \varepsilon_C. \tag{1}$$

In Eq. 1, a_C is a $p \times 1$ complex-valued observed vector, X_C is a $p \times q$ complex-valued known design matrix, β_C is a $q \times 1$ complex-valued unobserved regression coefficient vector, and ε_C is a complex-valued measurement error vector with same dimension as vector a_C, where p is the number of observations, and q is the number of regression coefficients. Moreover, the real and imaginary component of the measurement error ε_C follow normal distribution with $\varepsilon_R, \varepsilon_I \sim N(0, \sigma^2 I_p)$. In the application of this study, a_C is the complex-valued observed coil measurements vector, X_C is the complex-valued observed coil sensitivity matrix, and β_C is the unobserved voxel values vector. Eq. 1 can be reformulated through a real-valued isomorphism to transform the complex-valued model into a real-valued model:

$$\begin{bmatrix} a_R \\ a_I \end{bmatrix} = \begin{bmatrix} X_R & -X_I \\ X_I & X_R \end{bmatrix} \begin{bmatrix} \beta_R \\ \beta_I \end{bmatrix} + \begin{bmatrix} \varepsilon_R \\ \varepsilon_I \end{bmatrix}. \tag{2}$$

In Eq. 2, the dimension of observation vector $a = [a_R; a_I]$ is $2p \times 1$, the dimension of design matrix $X = [X_R, -X_I; X_I, X_R]$ is $2p \times 2q$, the dimension of regression coefficient vector $\beta = [\beta_R; \beta_I]$ is $2q \times 1$, and the dimension of measurement error vector $\varepsilon = [\varepsilon_R; \varepsilon_I]$ is $2p \times 1$. Thus, the likelihood distribution of the multivariate observation is:

$$P(a \mid X, \beta, \sigma^2) \propto (\sigma^2)^{-\frac{2p}{2}} \exp\left[-\frac{1}{2\sigma^2}(a - X\beta)'(a - X\beta)\right], \tag{3}$$

with independent and identical distributed (*iid*) observation, error for the normal distribution $a \sim N(X\beta, \sigma^2 I_{2p})$. In the linear regression model, the regression coefficients (voxel values) can be estimated through maximum likelihood estimation (MLE):

$$\hat{\beta}_{MLE} = (X'X)^{-1}X'a. \tag{4}$$

And the estimated variance through MLE is:

$$\hat{\sigma}^2_{MLE} = \frac{1}{2p}(a - X\hat{\beta})'(a - X\hat{\beta}). \tag{5}$$

To enhance anatomical detail and improve the resolution of reconstructed images, calibration images can be incorporated as prior information. The Tikhonov regularization algorithm has been shown to effectively increase the signal-to-noise ratio (*SNR*) (Lin et al. [12]). However, careful selection of the regularization parameter λ is crucial for optimal performance. In this paper, we propose a Bayesian complex-valued image reconstruction algorithm. Compared with Tikhonov regularization, the Bayesian framework enables principled use of calibration data and provides posterior estimates. This facilitates the construction of confidence intervals and hypothesis testing. As a result, inter-slice signal leakage can be eliminated, and correlations between reconstructed slices can be reduced. Based on prior knowledge and experience, the regression coefficient β (voxel values) is specified to have a normal prior distribution $P(\beta \mid \sigma^2)$, and the measurement error σ^2 is specified to have an inverse gamma prior distribution $P(\sigma^2 \mid \cdot)$. Thus, the posterior distribution of regression coefficient β and variance σ^2 is proportional to the joint distribution of the likelihood and the prior distributions:

$$P(\beta, \sigma^2 \mid \cdot) \propto P(a \mid X, \beta, \sigma^2)P(\beta \mid \sigma^2)P(\sigma^2 \mid \cdot). \tag{6}$$

The joint posterior distribution of the regression coefficient β (voxel values) and measurement error σ^2 can be integrated to obtain their marginal distributions and hence their marginal posterior mean (MPM) and variance. More details are provided in Section 2.

1.2. FMRI Background

In the functional magnetic resonance imaging (fMRI) study field, the topic of improving the efficiency of data acquisition in the image scanning process has been gaining researchers' interest since 1990. As a noninvasive medical imaging technique, the blood-oxygen-level dependent (BOLD) contrast signal is detected as the proxy reflecting neuron activation changes

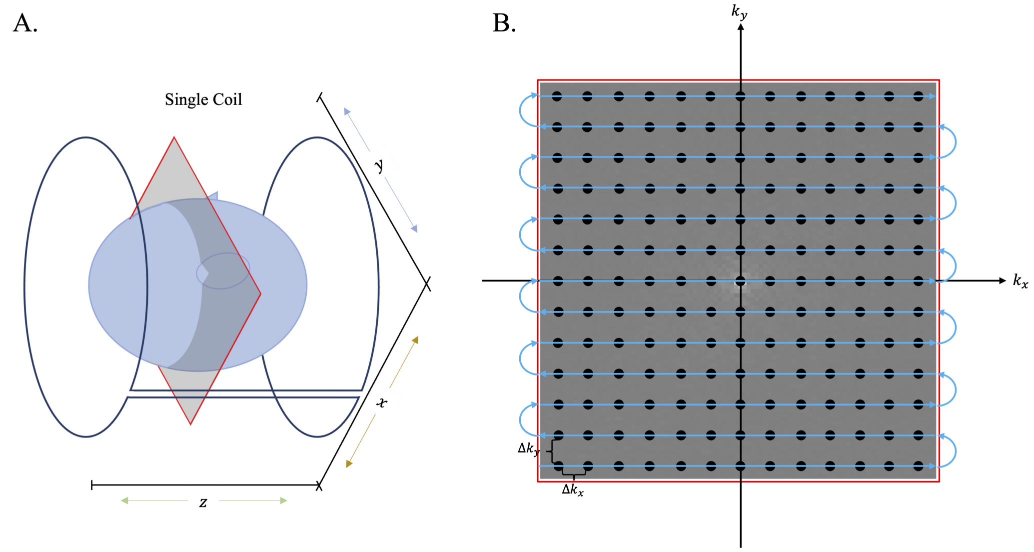

Figure 1: A. The three-dimensional view of brain image acquisition process with one single coil. B. The zig-zag data collecting pattern of GRE-EPI pulse sequence.

over time (Ogawa et al. [14]). In order to acquire the fully sampled spatial frequency space, known as k-space, the gradient echo echo-planar imaging (GRE-EPI) pulse sequence is applied to shorten the scan time and reduce the respiratory artifacts within a single excitation (Mansfield [13]; Redzian et al. [20]; Stehling et al. [24]). Fig. 1 illustrates a three-dimensional view of the brain image scanning process and the unique data acquisition sequential pattern in the k-space of the GRE-EPI pulse sequence (Sakitis et al. [21]). However, conducting an fMRI experiment requires acquiring multiple brain images at multiple slices, forming what is known as a volume-image.

In 1986, Hyde introduced a parallel image acquisition technique that incorporated multiple coils, with each coil measuring partial sensitivity-weighted spatial frequencies (Hyde et al. [7]). A full brain image can be reconstructed by applying the Sensitivity Encoding (SENSE) approach to combine weighted spatial frequencies from each coil into one single k-space array (Pruessmnn et al. [15]). In order to reduce the total image scan time, the data acquisition can be accelerated along two dimensions: the in-plane dimension and the through-plane dimension. The in-plane acceleration (IPA) method aims at expediting the single slice readout process by skipping partial lines in the k-space. As an alternative to SENSE, the unacquired spatial frequency

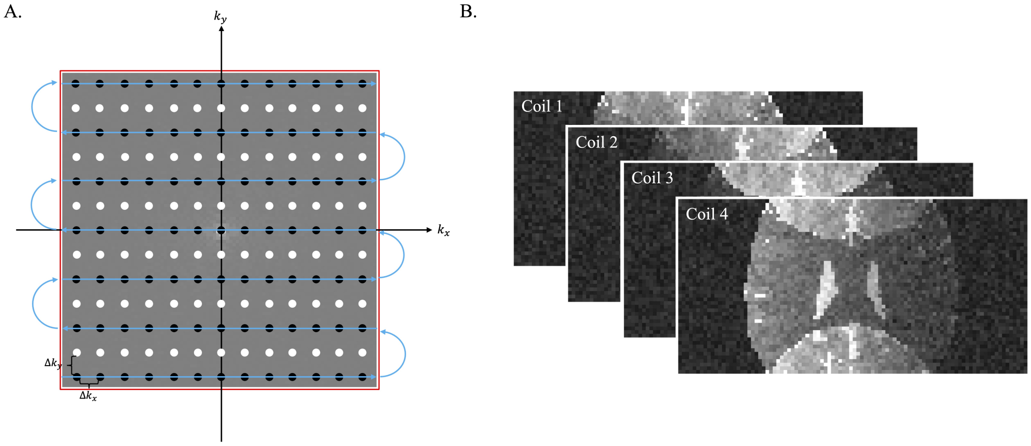

Figure 2: A. The subsampled spatial frequency domain incorporated with IPA approach and the acceleration factor equal to 2. B. The subsampled acquired images from four receriver coils.

points can be estimated by the application of the generalized autocalibrating partially parallel acquisition (GRAPPA) approach (Griswold et al. [6]). Prior information of missing data in the k-space can be obtained from the calibration images. Fig. 2A illustrates the brain image acquisition process with four receiver coils and the subsampled spatial frequency domain for IPA approach with acceleration factor IPA=2 (Sakitis et al. [21]). However, the total scan time does not decrease proportionally to the IPA factor due to fixed time blocks in the data acquisition process, such as proper time to form T_2^* contrast and imaging encoding time in a single excitation. The through-plane acceleration (TPA) approach, on the other hand, accelerates the image acquisition process by acquiring multiple slices simultaneously in one excitation. Techniques such as the simultaneous multi-slice (SMS) approach can be incorporated with the TPA approach by applying a multiband (MB) radiofrequency (RF) pulse within a reduced repetition time (TR) (Souza et al. [23]; Rowe et al. [19]; Barth et al. [1]; Rowe et al. [17]; Xu and Rowe. [26]). Compared to the IPA approach, the TPA approach significantly improves the efficiency of data acquisition, as the total scan time is reduced by a fraction corresponding to the TPA acceleration factor.

To further reduce the total image scan time and achieve the ultimate goal of our study, we introduce a novel SMS image reconstruction technique called “a controlled aliasing in parallel imaging with view angle tilting approach and in-plane acceleration method for multi-coil separation of parallel encoded complex-valued slices" (mSPECS-IPA-CAIPIVAT), which will be presented and discussed. This approach builds upon the mSPECS-IPA method by integrating both TPA and IPA acceleration techniques into a unified 2D acceleration technique (Kociuba [9]). By leveraging 2D acceleration, a higher acceleration factor can be achieved. In this novel image reconstruction method, we incorporate an image shift technique into the model to reduce the similarity of coil sensitivity information for aliased voxels, thereby improving image reconstruction accuracy.

2. Theory

2.1. The Data Acquiring Process

2.1.1. Image Shift Techniques

As discussed in Section 1.2, the SMS technique enables the concurrent acquisition of multiple brain slice images, reducing the total volume scan time depending on the selected TPA factor. Fig. 3 illustrates both 3D and 2D views of the image acquisition process with four slices and four coils. Unlike single-slice acquisition, multi-slice acquisition results in a short physical distance between aliased images. When applying the SENSE algorithm to reconstruct brain images and capture activity signals, an ill-conditioned matrix problem arises due to the high similarity of coil sensitivity information between closely spaced aliased voxels. Consequently, strong inter-slice signals and anatomical structures from other slices may appear as artifacts in the reconstructed images. To eliminate those wrong anatomical artifacts from other slices on the reconstructed brain images, decreasing the similarity of the coil sensitivity information is the primary strategy. Therefore, we introduced the images shift techniques to manually increase the physical distance between aliased images. To assess the performance of the image reconstruction method at high acceleration factors, we define the noise amplification factor, also known as the geometry factor (g-factor), as described in (Setsompop et al. [22]; Welvaert and Rosseel. [25]):

$$g_{SMS} = \frac{SNR_{full}}{SNR_{accelerate}\sqrt{R}}. \tag{7}$$

In Eq. 7, SNR_{full} is the signal-to-noise (SNR) ratio for the reconstructed images from techniques without acceleration factors and image shift techniques,

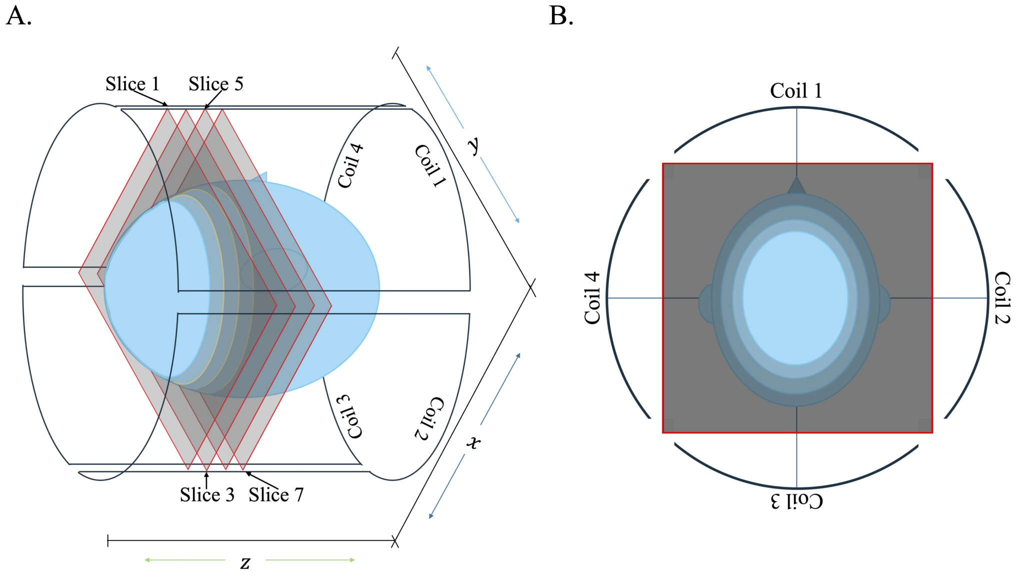

Figure 3: A. The 3D view of SMS technique with four slices and four coils acquisition process at one excitation. B. The 2D view for the same process with four slices and four coils.

and it can be assessed from the calibration images. $SNR_{accelerate}$ is the SNR value for the reconstructed images with acceleration factors, and the IPA acceleration factor R indicates the omission of spatial frequency data along the phase encoding direction. The closer the value of g_{SMS} is to 1, the better the reconstruction quality of the accelerated method. According to Eq. 7, high similarity of coil sensitivity information induces the high g_{SMS} value, which leads to a reduction of the $SNR_{accelerate}$ for the reconstructed images. Thus, to increase the $SNR_{accelerate}$ value and improve the performance of the novel acceleration technique, three image shift techniques have been incorporated.

In fMRI studies, the brain image can be shifted along three directions: the phase-encoding (PE) direction (vertically in this study), the readout (RO) direction (horizontally in this study), and PE and RO direction concurrently (vertically and horizontally at the same time in this study). To decrease the influence of the geometric properties of the coil sensitivity maps, techniques like “controlled aliasing in parallel imaging results in higher acceleration” (CAIPIRINHA) and “blipped-CAIPIRINHA” (Blipped-CAIPI) provide other possible ways to minimize the influence of the g-factor and maximize the physical distance of the aliased voxels (Breuer et al. [2]; Setsompop et al. [22]). The CAIPIRINHA approach can shift the images along the PE direction by modulating the phase for each line in the k-space and imparting each line with a specific phase. Applying a unique phase modulation amount to each slice in the aliased image-acquiring process increases the physical distance between the aliased voxels. Therefore, the independence of coil sensitivity for each slice will increase, and the influence of the g-factor for each excitation will be minimized. Moreover, to shift the brain image along the RO direction, a technique like the view angle tilting (VAT) approach applies compensation gradients to the slice selection direction to correct the chemical-shift artifacts in the image scanning process (Cho et al. [3]; Kim et al. [11]). The distance shifted along the RO direction is related to the view angle θ in the data acquisition process. The CAIPIRINHA and the VAT technique can be combined, and thus the study "multislice CAPIPRINHA using view angle tilting technique" (CAIPIVAT) proposed (Jungmann et al. [8]; Kim et al. [10]). Through this technique, the field-of-view (FOV) can be shifted along the PE and RO direction by applying different amounts of phase modulation to each line in the k-space and the compensation gradients on the slice selection direction together for each excitation. The GRE-EPI pulse sequence of the CAIPIRINHA, Blipped-CAIPI, and CAIPIVAT models could be investigated according to their respective references. Although the Blipped-CAIPI method conjuncts the VAT and the Hadamard encoding techniques, to further increase the diversity of the information in the image acquisition process, we introduced the 2D Hadamard phase encoding technique and discussed the combination with CAIPIRINHA, VAT and CAIPIVAT technique. Fig. 4 shows the k-space for CAIPIRINHA, VAT and CAIPIVAT techniques along the reconstructed brain images after the inverse Fourier transform.

2.1.2. 2D Hadamard Phase Encoding

The traditional Hadamard encoding technique is a well-developed volume-image method and widely used in fMRI studies (Souza et al. [23]). The conventional magnetic resonance (MR) imaging techniques have been limited by the size of the matrix for the acquired aliased images. The traditional Hadamard phase encoding method allows the increment of the size of the acquired aliased image matrix by aliasing in both frequency and phase encoding dimensions. With the support of this simultaneous binary-encoded technique, the TR will decrease, and the *SNR* ratio will improve. The Hadamard

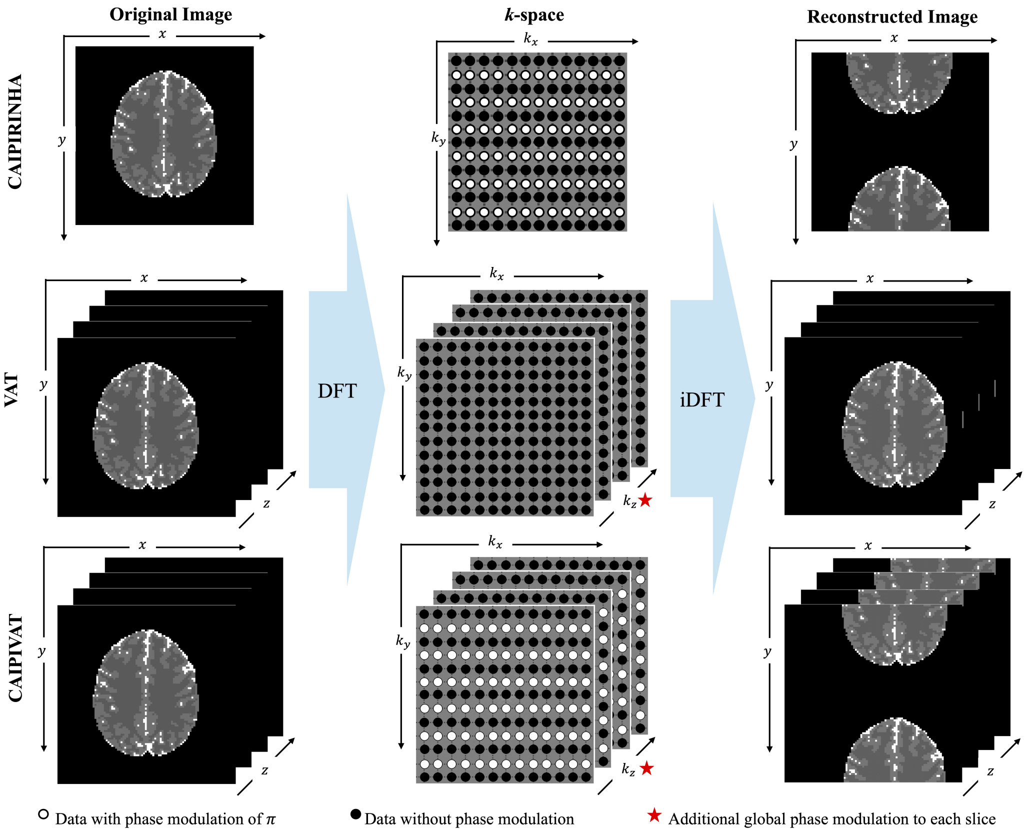

Figure 4: Top row: the image shift process corresponding to the CAIPIRINHA technique (shifted vertically). Middle row: the image shift process corresponding to the VAT technique (shifted horizontally). Bottom row: the image shift process corresponding to the CAIPIVAT technique (shifted vertically and horizontally).

matrix is given by:

$$H_{2^n} = \begin{bmatrix} H_{2^{n-1}} & H_{2^{n-1}} \\ H_{2^{n-1}} & -H_{2^{n-1}} \end{bmatrix} = H_2 \otimes H_{2^{n-1}}, \text{where } H_1 = \begin{bmatrix} 1 \end{bmatrix}, H_2 = \begin{bmatrix} 1 & 1 \\ 1 & -1 \end{bmatrix}, \tag{8}$$

where $\otimes$ denotes the Kronecker product. It is an orthogonal and full rank matrix with elements of either $+1$ or -1. The Hadamard phase encoding technique can be applied not only to through-plane imaging scenario but also to within-plane imaging scheme. The entire FOV can be divided into various regions of interest by applying Walsh functions during the pre-encoding section to define the frequency profile that the Hadamard pulses must follow (Fletcher et al. [5]).

In this study, since the TPA approach and the IPA approach are combined to further decrease the total image scan time, and the image shift techniques are incorporated to decrease the influences of the geometry properties, we introduce a novel 2D Hadamard phase encoding technique to our approach. The novel 2D Hadamard phase encoding technique is developed and based upon the Hadamard phase encoding technique with elements of either $+1$ or -1. However, different from the traditional Hadamard phase encoding technique, in order to guarantee the orthogonality property for each aliased image, different 2D Hadamard coefficients will be assigned to different segments for different slices. Fig. 5 shows the 2D Hadamard phase encoding aliasing coefficient for $N_s = 2$ and $N_s = 4$ situations, where N_s is the number of aliased slices for each excitation. First, for each excitation or each TR, the through-plane Hadamard coefficient will be assigned to different slices. Second, for each segment of each slice, the in-plane Hadamard coefficient will be assigned to a different excitation. To maintain the orthogonality property for each segment of each slice, the in-plane Hadamard coefficient starts from the second column of the Hadamard coefficient for the first excitation. At the last TR of the cycle, the in-plane Hadamard coefficient is the first column of the Hadamard matrix. Finally, the 2D Hadamard coefficient will be the product of the through-plane and in-plane Hadamard coefficient for each segment of each slice and each excitation. The size of the in-plane and through-plane Hadamard coefficient matrix is equal to the number of aliased slices, N_s, for each excitation.

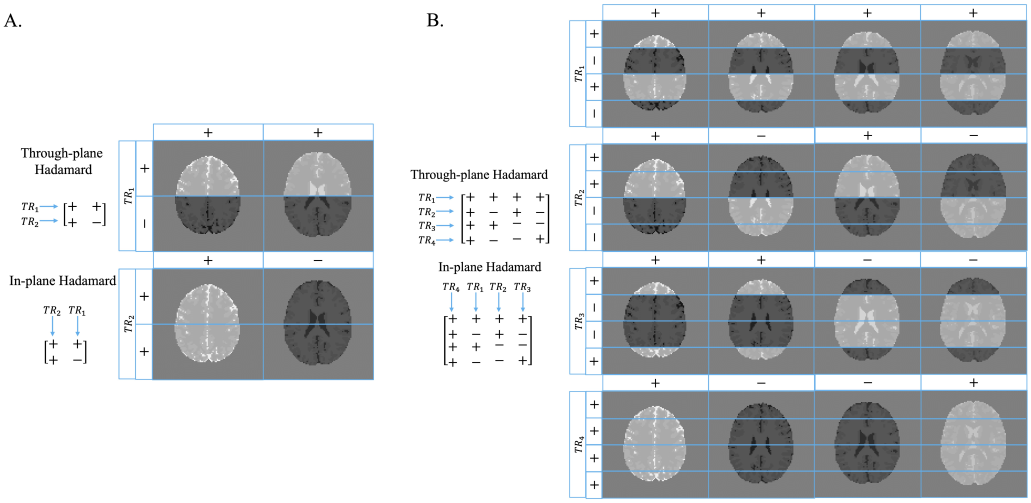

Figure 5: A. The 2D Hadamard phase encoding coefficient for $N_s = 2$. B. The 2D Hadamard phase encoding coefficient for $N_s = 4$.

2.1.3. The Combination of Image Shift Techniques and 2D Hadamard Phase Encoding

To accomplish the goal of decreasing the coil sensitivity information similarity of aliased voxels, and thus decreasing the influence of the g-factor, we combined the image shift techniques and the 2D Hadamard phase encoding technique together. Fig. 6 shows the image shift situation corresponding to different SMS techniques for the first 4 TRs along with the 2D Hadamard coefficients for each segment of the slices under the circumstance with $N_s = 4$. Compared with the mSPECS-IPA method (Fig. 6A), the other three methods are incorporating with different image shift directions and amount for each slices and each excitation. Fig. 6B shows the image shift situation along with the 2D Hadamard coefficients incorporating with the mSPECS-IPA-CAIPIRINHA method. For each slice within each TR, a $\Delta y = (l-1)FOV/N_s$ of in-plane image shift on the vertical direction will be implied, where $l = 1, \ldots, N_s$. For each excitation, a $\Delta y = (m-1)FOV/N_s$ of in-plane image shift on the vertical direction will be implied, where $m = 1, \ldots, N_s$. Thus, with the in-plane and the through-excitation CAIPIRINHA image shift, the voxel aliasing situation at $TR_{N_s}+1$ will be identically same as aliasing situation at TR_1. Fig. 6C shows the image shift situation along with the two-dimensional Hadamard coefficients incorporating with the mSPECS-IPA-VAT method. Unlike the mSPECS-IPA-

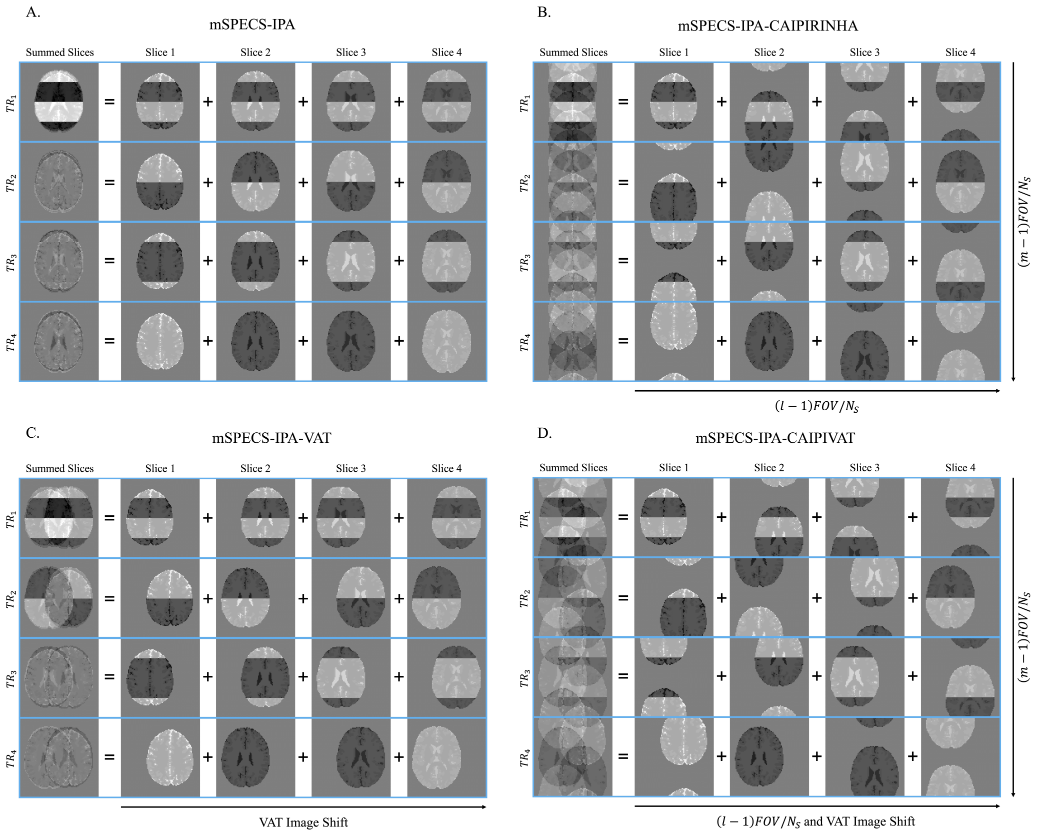

Figure 6: The voxel aliasing situation for the first 4 TRs with $N_s = 4$ circumstance incorporating with A. mSPECS-IPA image shift technique, B. mSPECS-IPA-CAIPIRINHA technique, C. mSPECS-IPA-VAT technique, and D. mSPECS-IPA-CAIPIVAT technique.

CAIPIRINHA method, the mSPECS-IPA-VAT method only shift the image along the horizontal direction. Thus, for each excitation and each slice, no image shift happens along the vertical direction, but a modest amount of image shift will be applied for each slice and each excitation along the horizontal direction. Fig. 6D shows voxel aliasing situation incorporated with the mSPECS-IPA-CAIPIVAT method. Since the mSPECS-IPA-CAIPIVAT method is combining the principle idea of mSPECS-IPA-CAIPIRINHA and mSPECS-IPA-VAT method together, the image shift will happen along the vertical and the horizontal direction. For each slice within each excitation, a $\Delta y = (l-1)FOV/N_s$ amount of the image shift along the vertical direction, where $l = 1, \ldots, N_s$, and the amount of the image shift technique

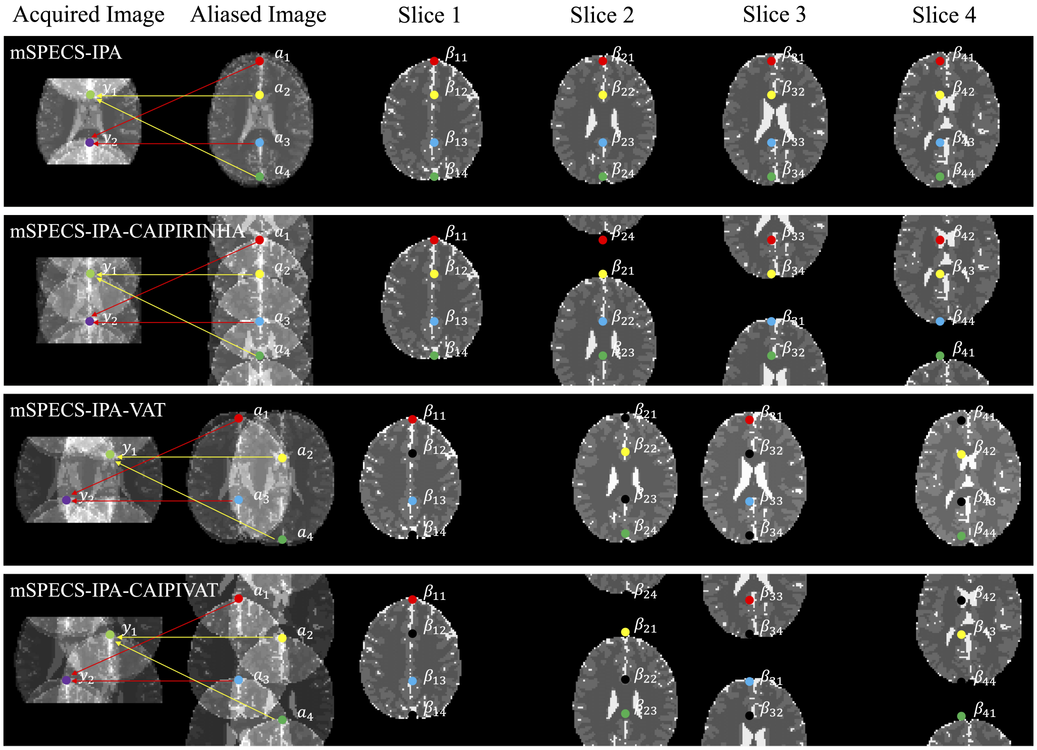

Figure 7: The voxel aliasing situation with $N_s = 4$ for mSPECS-IPA, mSPECS-IPA-CAIPIRINHA, mSPECS-IPA-VAT and mSPECS-IPA-CAIPIVAT technique.

corresponding to the VAT technique along the horizontal direction will be implied. Moreover, for each excitation, a $\Delta y = (m-1)FOV/N_s$ of through-excitation image shift will be implied along the vertical direction, where $m = 1, \ldots, N_s$. In real-world volume image acquisition, the 2D Hadamard phase-encoding technique should be applied before the image shift techniques (Fletcher et al. [5]). A careful design of the Hadamard pre-encoding process is necessary to ensure the orthogonality of the 2D Hadamard aliasing coefficients. Comparing these four image shift techniques, the overlapping area between summed slices are decreasing from the mSPECS-IPA method to the mSPECS-IPA-CAIPIVAT method. However, since the novel proposed SMS technique is aiming at combining TPA and IPA technique together, thus, making the voxel aliasing situation clear after the IPA technique is another vital process to discuss in this paper.

Fig. 7 displays the voxel aliasing situation after the IPA aliasing technique for mSPECS-IPA, mSPECS-IPA-CAIPIRINHA, mSPECS-IPA-VAT, and mSPECS-IPA-CAIPIVAT technique under the circumstance with $N_s = 4$. In Fig. 7, those dots in the same color indicating voxels are aliased together. From the top model to the bottom model, the physical distance between aliased voxels increases, leading to reduced coil information similarity and, consequently, a lower g-factor. Moverover, comparing the mSPECS-IPA and the mSPECS-IPA-CAIPIRINHA method, after the IPA acceleration technique, the mSPECS-IPA-CAIPIRINHA has the more complex aliasing artifacts and the overlapping area is larger than the mSPECS-IPA method especially at the center part of the acquired images. Comparing the bottom two methods, mSPECS-IPA-VAT and the mSPECS-IPA-CAIPIVAT technique, the similar conclusion can be made. In this work, the combination of image shift techniques and 2D Hadamard phase encoding was not implemented experimentally, as this is a methodological study. Instead, we utilized fully sampled k-space data, and the slices were artificially Hadamard encoded and aliased.

2.2. A Single Aliased Voxel

Given an excitation δ in the fMRI time series, we define $IS_{\delta,z}$ notation indicating the image shift pattern for the zth slice and the δth TR, corresponding to one of the mSPECS-IPA, mSPECS-IPA-CAIPIRINHA, mSPECS-IPA-VAT and the mSPECS-IPA-CAIPIVAT technique, and it follows the definition in Section 2.1.1. Thus, for a single aliased voxel at the location (x, y) of the acquired aliased images with TPA and IPA acceleration techniques, corresponding to the 2D Hadamard coefficients at time point δ, measured at jth coil, is defined as the summation equation:

$$a_{j,\delta} = \sum_{k=1}^{IPA} \sum_{z=1}^{N_s} H_{\delta,z,k} S_{IS_{\delta,z},k} \beta_{IS_{\delta,z},k} + \varepsilon_{j,\delta}. \tag{9}$$

In Eq. 9, the acquired aliased voxel value $a_{j,\delta}$ is a complex-valued data with real and imaginary component, $a_C = a_R + ia_I$, and parameter k is the IPA indicator. The 2D Hadamard coefficient, $H_{\delta,z,k}$, is a real-valued orthogonal matrix corresponding to the δth excitation, zth slice and the kth IPA process, and it strictly follows the definition of the 2D Hadamard phase encoding in Section 2.1.2. All of the element of the $H_{\delta,z,k}$ coefficient matrix is either $+1$ or -1. The coil sensitivity information matrix, $S_{IS_{\delta,z},k}$, is a complex-valued data point with real and imaginary component, $S_C = S_R + iS_I$, corresponding to the kth IPA process and the image shift process at δth excitation and zth slice. The true voxel value, $\beta_{IS_{\delta,z},k}$, is a complex-valued data point with real and imaginary component, $\beta_C = \beta_R + i\beta_I$, corresponding to the kth IPA process and the image shift process at δth excitation and zth slice. The measurement error, $\varepsilon_{j,\delta}$, is also a complex-valued data point with real and imaginary component, $\varepsilon_C = \varepsilon_R + i\varepsilon_I$, corresponding to the δth time point and jth coil. Moreover, the real and imaginary component of measurement error is specified to be a normal distribution with mean $E(\varepsilon_R, \varepsilon_I) = 0$ and variance $var(\varepsilon_R, \varepsilon_I) = \sigma^2$.

Considering the acquired aliased voxel in Eq. 9 across total N_c coils, N_α time points and the N_s slices in the whole fMRI time series, the real-valued isomorphic representation of Eq. 9 can be expressed similar to Eq. 1:

$$a = X_A\beta + \varepsilon. \tag{10}$$

In Eq. 10, $a = [a_R; a_I]$ is a real-valued vector with dimension $2N_cN_\alpha \times 1$. The real-valued aliasing matrix $X_A = [(X_A)_R, -(X_A)_I; (X_A)_I, (X_A)_R]$ is known prior information including the 2D Hadamard coefficients and the coil sensitivity information across the N_c coils, N_α time points and the N_s slices. Thus, the dimension of the aliasing matrix X_A is $2N_cN_\alpha \times 2N_s$. For the δth excitation, the known aliasing matrix $(X_A)_\delta$ across N_c coils and N_s slices is defined as:

$$(X_A)_\delta = \left[H_{\delta,1} \begin{pmatrix} S_{1,1} \\ \vdots \\ S_{N_c,1} \end{pmatrix}, \dots, H_{\delta,N_c} \begin{pmatrix} S_{1,N_s} \\ \vdots \\ S_{N_c,N_s} \end{pmatrix} \right]. \tag{11}$$

Across the N_α excitations, the Eq. 11 can be expressed as:

$$X_A' = \left[(X_A)_1', \dots, (X_A)_{N_\alpha}' \right]. \tag{12}$$

The true voxel value in Eq. 10, $\beta = [\beta_R; \beta_I]$, is a vector we want to estimate, with dimension $2N_s \times 1$. The measurement error in Eq. 10, $\varepsilon = [\varepsilon_R; \varepsilon_I]$ has the same dimension as the a vector. The real and imaginary component of the measurement error is specified to be normal distributed with mean $E(\varepsilon) = 0$ and covariance $cov(\varepsilon) = \sigma^2 I_{2N_cN_\alpha}$, where $I_{2N_cN_\alpha}$ is the identity matrix.

Thus, in order to separate the aliased images and estimate the true voxel value for each slice, the maximum likelihood estimation in Eq. 4 can be applied and the estimated voxel value, $\hat{\beta}_{MLE}$, can be calculated by:

$$\hat{\beta}_{MLE} = \left(X_A^{'} X_A\right)^{-1} X_A^{'} a. \tag{13}$$

Moreover, the covariance of the voxel value $\hat{\beta}$, can be estimated by:

$$cov(\hat{\beta}_{MLE}) = \sigma^2 \left(X_A^{'} X_A\right)^{-1}. \tag{14}$$

According to the methodology of the combination of image shift techniques and the 2D Hadamard phase encoding technique, the novel proposed SMS method accelerates the image acquiring process along the TPA and the IPA dimension. However, the relative short scan time leads to the less data information collected during the image acquiring process compared with the traditional imaging technique without acceleration techniques. Furthermore, it also leads to the ill-condition of the designed aliasing matrix which will cause failure to calculate the inverse of $X_A^{'} X_A$. Thus, coming up with a technique that is capable to fix the ill-condition designed matrix problem and hence calculate the inverse problem is the next priority. In this study, we introduced the bootstrap sampling technique along with the artificial aliasing of the calibration images technique to solve this problem. By applying these two techniques into the novel image shift SMS technique, the designed aliasing matrix is made to be full rank and invertible and the inter-slice signal leakage can be eliminated.

2.3. The Bootstrap Sampling and Artificial Aliasing of Calibration Images

Based on the discussion in the previous sections, to make the designed aliasing matrix to be full rank and invertible, slices information from the calibration images can be utilized as the reference information. The bootstrap sampling technique is a widely used tool which can decrease the correlation induced by the image separation process and eliminate the inter-slice signal leakage. In the image separation process, for each excitation, the bootstrap sampling technique will be applied to the calibration images. The bootstrapping size for each excitation is related to the TPA factor, which is equal to the number of aliased slices for each excitation and the IPA factor. Thus, for each excitation in the fMRI time series, $N_s R$ bootstrapped sampled slices will be randomly chosen from the fully sampled calibration image time series. The randomly chosen slices will be averaged and the mean calibration images will be utilized for the artificial aliasing process.

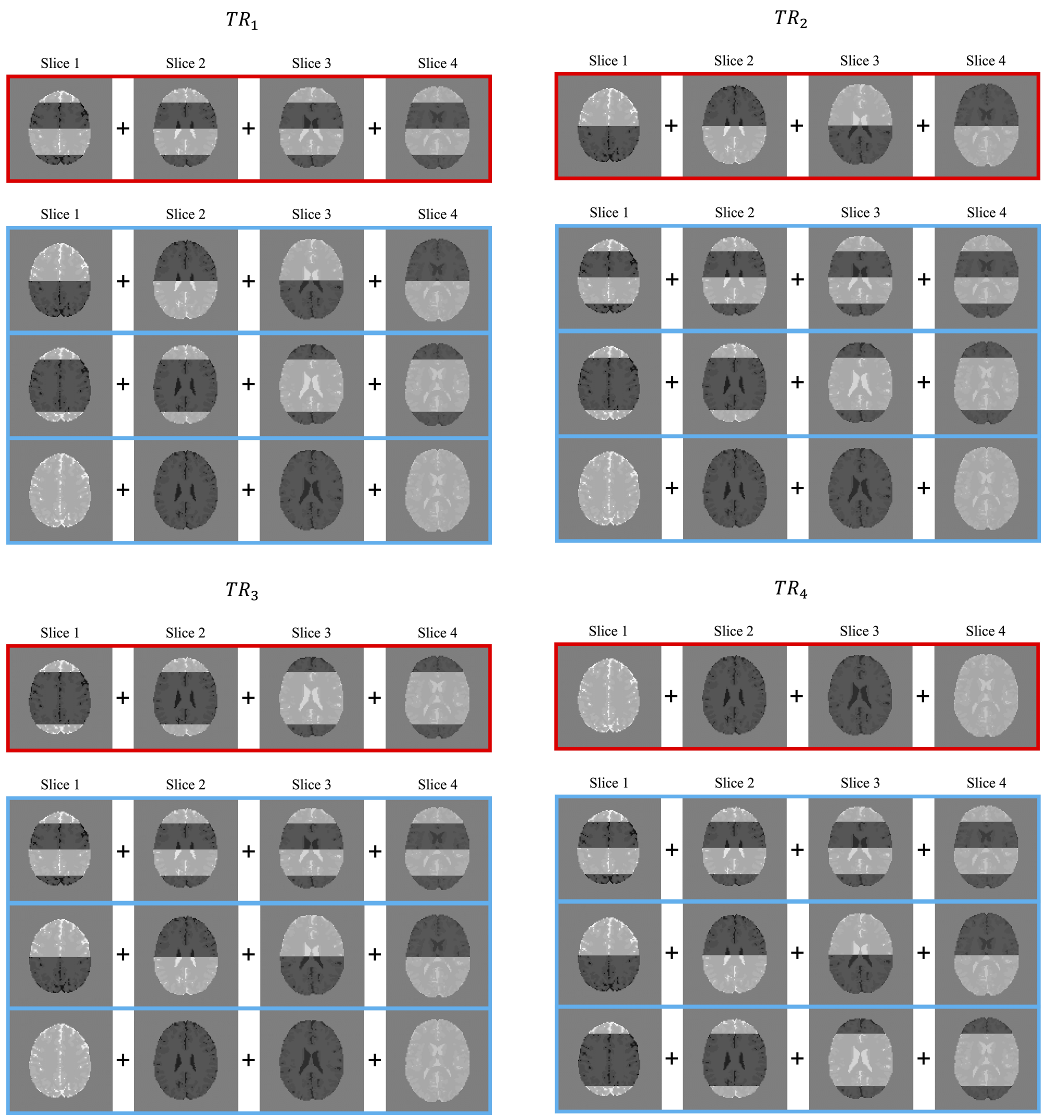

Figure 8: The the 2D Hadamard aliasing coefficients for acquired aliased slices (red box) and the artificial aliased calibration slices (blue box) for the first 4 TRs with $N_s = 4$.

For each excitation, the same image shift pattern will be applied to both acquired aliased images and the artificial aliased calibration images. But different 2D Hadamard aliasing coefficient matrix will be applied to acquired aliased images and the artificial aliased calibration images. Fig. 8 shows the 2D Hadamard aliasing coefficient for acquired aliased slices (red box) and the artificial aliased calibration slices (blue box) for the first 4 TRs with $N_s = 4$. For each segment of each slice, the white part means the Hadamard coefficient is $+1$, and the black part means the Hadamard coefficient is -1. Moreover, the 2D Hadamard aliasing coefficient for acquired aliased slices and artificial aliased calibration slices at time point TR_{N_s+1} will be identical as TR_1. Based on the 2D Hadamard aliasing coefficients for acquired aliased slices and the artificial aliased calibration slices, for each excitation, $N_s - 1$ combinations of 2D Hadamard aliasing coefficient remain for the artificial aliasing process.

Similar to Eq. 10, for a single excitation, a single voxel, ν, from the artificial aliasing calibration aliased slices located at (x, y) across N_s slices, measured through N_c coils can be expressed as:

$$\nu = C\bar{\nu} = C_A\mu + C\eta. \tag{15}$$

In Eq. 15, the artificial aliased voxel value, $\nu = [\nu_R; \nu_I]$, is a vector with real and imaginary component and dimension $2N_sN_c(N_s - 1) \times 1$. The mean bootstrap sampled voxel, $\bar{\nu} = [\bar{\nu}_R; \bar{\nu}_I]$, is a vector with dimension $2N_s \times 1$. The true calibration voxel value, $\mu = [\mu_R; \mu_I]$, and the measurement error, $\eta = [\eta_R; \eta_I]$, have the same dimension with the mean bootstrap sampled voxel vector. Moreover, the mean of the measurement error is $E(C\eta) = 0$ and covariance is $cov(C\eta) = \tau^2 I_{2N_sN_c(N_s-1)}$ where $I_{2N_sN_c(N_s-1)}$ is the identity matrix. If the bootstrap sampling technique does not incorporate, *i.e.* the same calibration images are keep using into the model, then the covariance of the measurement error is $\tau^2 = 0$, thus the correlation between the reconstructed slices is induced by the image separation process. However, under the assistance of the bootstrap sampling technique, $\tau^2 = \sigma^2$, and the covariance of the measurement error of the calibration image is $cov(C\eta) = \sigma^2 I_{2N_sN_c(N_s-1)}$.

The artificial aliasing matrix, C_A in Eq. 15, is a known prior information including the 2D Hadamard coefficients for the artificial aliasing slices and the coil sensitivity information across N_c coils, N_α time points and N_s slices. Thus, the dimension of the artificial aliasing matrix, C_A, is $2N_sN_c(N_s - 1) \times 2N_s$. For the δth excitation, the known artificial aliasing matrix $(C_A)_\delta$ across N_c coils and N_s slices is defined as:

$$(C_A)_\delta = \left[\overline{H_{\delta,1}} \begin{pmatrix} S_{1,1} \\ \vdots \\ S_{N_c,1} \end{pmatrix}, \ldots, \overline{H_{\delta,N_c}} \begin{pmatrix} S_{1,N_s} \\ \vdots \\ S_{N_c,N_s} \end{pmatrix} \right]. \tag{16}$$

The notation $\overline{H}$ indicates the remaining 2D Hadamard aliasing coefficient for each excitation after removing the 2D Hadamard aliasing coefficient for the acquired aliased images. Across the N_α excitations, the Eq. 16 can be expressed as:

$$C_A' = \left[(C_A)_1', \ldots, (C_A)_{N_\alpha}' \right]. \tag{17}$$

2.4. The Likelihood, Prior, and Joint Distribution

As discussed in Section 1.1, the acquired aliased voxel values across the whole brain image are independent and identically distributed and the measurement error for each acquired aliased voxel is specified to be Gaussian distributed. Thus, the likelihood distribution (Eq. 3) of the acquired aliased voxel is:

$$P(a \mid X_A, \beta, \sigma^2) \propto (\sigma^2)^{-\frac{2N_c N_\alpha}{2}} \exp\left[-\frac{1}{2\sigma^2}(a - X_A\beta)'(a - X_A\beta) \right]. \tag{18}$$

Following the methodology of the Bayesian approach, the voxel value from calibration images can be utilized as prior information. Moreover, in Section 1.1 the voxel value, β, is specified to have a normal prior distribution. Therefore, the prior distribution of the voxel value $\beta \sim N(\mu, \sigma^2(C_A' C_A)^{-1})$:

$$P(\beta \mid C_A, \mu, \sigma^2) \propto (\sigma^2)^{-\frac{2N_s N_r}{2}} \exp\left[-\frac{1}{2\sigma^2}(\beta - \mu)'(C_A' C_A)(\beta - \mu) \right]. \tag{19}$$

Moreover, in Section 1.1, the variance of the measurement error, σ^2 is specified to have an inverse gamma prior distribution:

$$P(\sigma^2 \mid \lambda, \delta) \propto (\sigma^2)^{-(\lambda+1)} \exp\left[-\frac{\delta}{\sigma^2} \right], \tag{20}$$

where hyperparameters μ, λ and δ are assessed from the calibration images. The posterior distribution of the voxel value, β, and the variance of the measurement error, σ^2, follows the joint distribution as Eq. 6:

$$P(\beta, \sigma^2 \mid \cdot) \propto P(a \mid X_A, \beta, \sigma^2) P(\beta \mid C_A, \mu, \sigma^2) P(\sigma^2 \mid \lambda, \delta). \tag{21}$$

2.5. Hyperparameters Assessment

Before the image acquisition process of the novel proposed SMS model, a time series of calibration images will be collected first. The calibration image time series will be acquired through the traditional fMRI technique, and unlike the novel SMS model incorporating with different image shift techniques and 2D Hadamard aliasing coefficient. The calibration image time series is acquired without any image shift techniques or aliasing coefficient, no task experiment will be executed during this time series. As discussed in Section 2.4, the calibration images can be utilized as prior information, hence the unknown hyperparameters can be assessed from calibration time series. In Eq. 21, the acquired aliasing matrix X_A and the artificial aliasing matrix C_A are known prior information that we do not need to assess from the calibration image time series. The hyperparameters μ, λ, and δ, on the other hand, need to be assessed from the calibration image time series. As discussed in Section 2.3, the hyperparameter μ is the averaged voxel value after the bootstrap resampling process. For each excitation in the time series, N_s brain images will be randomly chosen from the fully sampled calibration images and averaged to assess the hyperparameter averaged voxel value $\mu = \bar{\nu}$. The shape parameter λ and the scale parameter δ from inverse gamma distribution in Eq. 20, also need to be assessed from the calibration image time series. After the bootstrap resampling process, the sample noise variance σ_0^2 can be estimated from the calibration image time series. Thus, the shape parameter can be assessed by $\lambda = n_0$, and the scale parameter can be assessed by $\delta = (n_0 - 1)\sigma_0^2$, where n_0 is the number of calibration images and σ_0^2 is sample noise variance.

2.6. The Posterior Estimation

According to the discussion in Section 1.1, Section 2.4, and Section 2.5, the joint distribution (Eq. 21) of the likelihood distribution of acquired aliased (Eq. 18), the prior distribution of the voxel value β (Eq. 19), and the prior distribution of the noise variance σ^2 (Eq. 20) can be calculated after algebra:

$$\begin{aligned} &P(\beta, \sigma^2 \mid \cdot) \\ &\propto (\sigma^2)^{-\frac{p}{2}} \exp\left[-\frac{1}{2\sigma^2}((\beta - \hat{\beta}_{MPM})'(X_A^{'} X_A + C_A^{'} C_A)(\beta - \hat{\beta}_{MPM}) + w)\right], \end{aligned} \tag{22}$$

where $p = 2N_c N_\alpha + 2N_s N_r - 2\lambda - 2$, and $w = a^{'} a + \mu^{'} C_A^{'} C_A \mu - (X_A^{'} a + C_A^{'} C_A \mu)^{'} (X_A^{'} X_A + C_A^{'} C_A)^{-1} (X_A^{'} a + C_A^{'} C_A \mu) + 2\delta$. Moreover, as discussed in Section 1.1, the posterior distribution of the voxel value, β, and the noise variance, σ^2 can be integrated through the MPM technique. Therefore, the marginal posterior distribution of estimate voxel value β after integration is a student-t distribution $\beta \sim t(\nu^\star)$:

$$f(\beta \mid \cdot) \propto \left\{ 1 + \frac{1}{\nu^\star}(\beta - \hat{\beta}_{MPM})' \left[\frac{(X_A' X_A + C_A' C_A)}{\tau^2} \right] (\beta - \hat{\beta}_{MPM}) \right\}^{\frac{\nu^\star + 1}{2}}, \tag{23}$$

with $\nu^\star = p - 1$ and $\tau^2 = w/\nu^\star$. The marginal posterior mean (MPM) for $\hat{\beta}$ after integration is:

$$E(\beta \mid \cdot) = \hat{\beta}_{MPM} = (X_A' X_A + C_A' C_A)^{-1}(X_A' a + C_A' C_A \mu). \tag{24}$$

In Eq. 24, the matrix $C_A' C_A$ acts as a regularizer for the matrix inverse to improve the condition of the equation. Since the true voxel value from calibration images is close to the true voxel value from acquired aliased images, Eq. 24 leads to $E(\beta \mid \cdot) = \beta$. The marginal posterior covariance of the voxel value $\hat{\beta}$ is:

$$cov(\beta \mid \cdot) = \frac{\nu^\star}{\nu^\star - 2} \tau^2 (X_A' X_A + C_A' C_A)^{-1}, \tag{25}$$

the separated voxel values are uncorrelated, meaning that there will not be signal leakage between slices.

Moreover, the marginal posterior distribution of σ^2 after integration is an inverse gamma distribution, $\sigma^2 \sim IG(\gamma, w/2)$:

$$f(\sigma^2 \mid \cdot) \propto (\sigma^2)^{-\frac{p}{2} - 1} \exp\left[-w/(2\sigma^2) \right], \tag{26}$$

with $\gamma = (p-1)/2$. The MPM of the noise variance σ^2 is:

$$E(\sigma^2 \mid \cdot) = \frac{w/2}{\gamma}, \tag{27}$$

and the marginal posterior variance of the noise variance is:

$$var(\sigma^2 \mid \cdot) = \frac{w/2}{(\gamma - 1)^2 (\gamma - 2)}. \tag{28}$$

3. FMRI Data

3.1. Simulated FMRI Data

The proposed novel image shifted SMS technique was first applied to simulated fMRI data. The reconstructed brain images were compared through

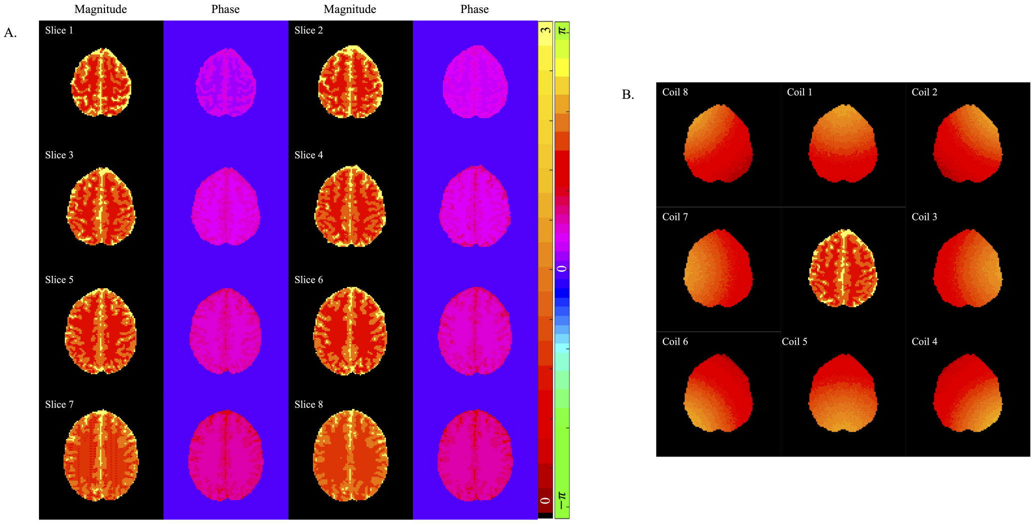

Figure 9: A. The magnitude and phase for the true noiseless simulated axial brain images with $N_s = 8$. B. The magnitude of the simulated sensitivity coils for slice 3 with $N_c = 8$.

the mSPECS-IPA model (non image shift technique), the mSPECS-IPA-CAIPIRINHA model (image vertically shift), the mSPECS-IPA-VAT model (image horizontally shift) and the mSPECS-IPA-VAT model (image vertically and horizontally shift). Our goal is to improve the efficiency of the image acquisition process while simultaneously determining which image shift direction provides the best reconstruction results.

The simulated fMRI time series is mimicking the real-world right hand finger tapping experiment with the total number of TR (repetition time) $= 510$. According to the methodology of the image shifted SMS technique, two separate fMRI time series need to be simulated: the acquired fMRI time series and the calibration fMRI time series. The acquired fMRI time series was simulated using the mSPECS-IPA, mSPECS-IPA-CAIPIRINHA, mSPECS-IPA-VAT, and mSPECS-IPA-CAIPIVAT models, as different image shift directions were applied. The calibration fMRI time series, however, was simulated without any image shift technique or acceleration techniques. The calibration images were reconstructed by applying SENSE model. Since the simulated fMRI time series mimics an *in vivo* experiment, the first 20 repetition times are omitted to achieve a steady magnetic field, leaving a total number of $TR = 490$. In the simulated fMRI time series, total $N_s = 8$ axial brain images were included in the acquired simulated fMRI time series and the calibration simulated fMRI time series. In the calibration simulated time series, no simulated task block were added to the brain images. On the other hand, the simulated task blocks were added to the left motor cortex of the top 4 brain images. The simulated task blocks were added according to the real-world right hand finger tapping experiment with 15 TRs off and 15 TRs on for 16 epochs, and the first 20 TRs and last 10 TRs off. The contrast-to-noise ratio and the signal-to-noise ratio we choose also mimick the real-world fMRI experiment and $SNR = 50$ and $CNR = 0.5$. Thus, the mean magnitude added to each simulated slice is 4 and the mean magnitude added to the simulated task blocks is 0.04. Moreover, a Gaussian distributed noise $N(0, 0.0064)$ was added to each slice of the simulated acquired fMRI time series and the simulated calibration fMRI time series. In order to increase the difference between each simulated slices, different phase angles from $5°$ to $40°$ with $5°$ intervals were added to each slice. Different phase angles were also added to different brain tissue with $7.5°$ for white matter (WM), $15°$ for gray matter (GM), and $22.5°$ for cerebral spinal fluid (CSF).

In order to investigate the performance of different model with different acceleration factor, the IPA factor we used in the simulated acquired fMRI dataset is $R = 2$, and different TPA factors were incorporated in the experiment with $TPA = 2$, $TPA = 4$, and $TPA = 8$. Thus, the net acceleration factor is the product of the IPA factor and the TPA factor with $NET = 4$, $NET = 8$, and $NET = 16$. For $TPA = 2$ situation, the slices aliasing situation is: packet 1: slice 1 and slice 5, packet 2: slice 2 and slice 6, packet 3: slice 3 and slice 7, packet 4: slice 4 and slice 8. For $TPA = 4$ situation, the slices aliasing situation is: packet 1: even slices, packet 2: odd slices. For $TPA = 8$ situation, all slices are aliased in one packet.

Fig. 9A shows the true noiseless magnitude and phase for each slice of simulated axial brain images with $N_s = 8$. A total number of $N_c = 8$ channel sensitivity coils were simulated and applied according to the real right hand finger tapping experiment. Fig. 9B shows the magnitude and position for each coil corresponding to slice 3. The mean magnitude for each simulated coil is 0.95, and to increase the difference between each coil, different phase angles were added to the simulated coils from $0°$ to $17.5°$ with $2.5°$ intervals.

The simulated SMS data used in this study were generated through artificial aliasing of fully sampled k-space data. While this approach allows controlled investigation of image shift direction, Hadamard encoding, and Bayesian regularization effects, it does not reproduce all characteristics of real SMS acquisitions, such as slice dependent phase errors, eddy current effects, and complex noise correlations. Therefore, the simulation results are intended to provide mechanistic insights into reconstruction behavior rather than a definitive performance comparison against established SMS reconstruction methods such as Slice-GRAPPA or Split Slice-GRAPPA, which have been extensively validated using in vivo multiband acquisitions (Cauley et al. [4]; Setsompop et al. [22]).

3.2. Experimental FMRI Data

A real-world right-handed finger tapping fMRI experiment for a single object was executed through a 3.0 T General Electric Signa LX MRI scanner. The flip angel was 90° and the acquisition bandwidth is 125 kHz in this experiment. The slice thickness for the axial brain images was 2.5 mm. A total of nine slices were scanned. In this experiment, an 8 channel receiver head coil was utilized with dimension 96×96 for a 24 cm full field-of-view, with the phase encoding direction from posterior to anterior. It should be noted that the 8 channel receiver coil used in this experiment provides limited spatial sensitivity variation for high through-plane acceleration factors. In current SMS fMRI practice, 32 channel or higher receiver arrays are typically employed to support robust slice separation. Consequently, the present dataset is not intended to demonstrate optimal SMS image quality, but rather to evaluate relative reconstruction behavior under constrained coil geometry. In the real-world right-handed finger tapping fMRI experiment, two fMRI time series were acquired: the non-task calibration time series and the task time series. The right-handed finger tapping experiment was designed with an initial 20 TRs off rest, followed by 15 TRs off and 15 TRs on for 16 epochs, and the final 10 TRs of rest, resulting in a total 510 TRs for the task time series. The same echo time (TE) information was applied to both fMRI time series, consisting of three segments. The TE for the first 10 TRs and the last 490 TRs was 42.7 ms. From the 11th to the 20th time point, the TE values were 42.7 ms, 45.2 ms, 47.7 ms, 50.2 ms, and 52.7 ms, and this sequence was repeated twice. The first 20 TRs of the task time series were disregarded to achieve a steady magnetic field of the scanner, resulting in last 490 TRs of the task time series were applied to the novel proposed model.

In the real-world right-handed finger-tapping fMRI experiment, aliased task images were not acquired experimentally, as this is a methodological study. Since the dimension of the 2D Hadamard aliasing coefficient must be a power of two, only eight slices were used in the proposed image-shifted SMS techniques, with the most interior axial brain slice disregarded. Instead, the

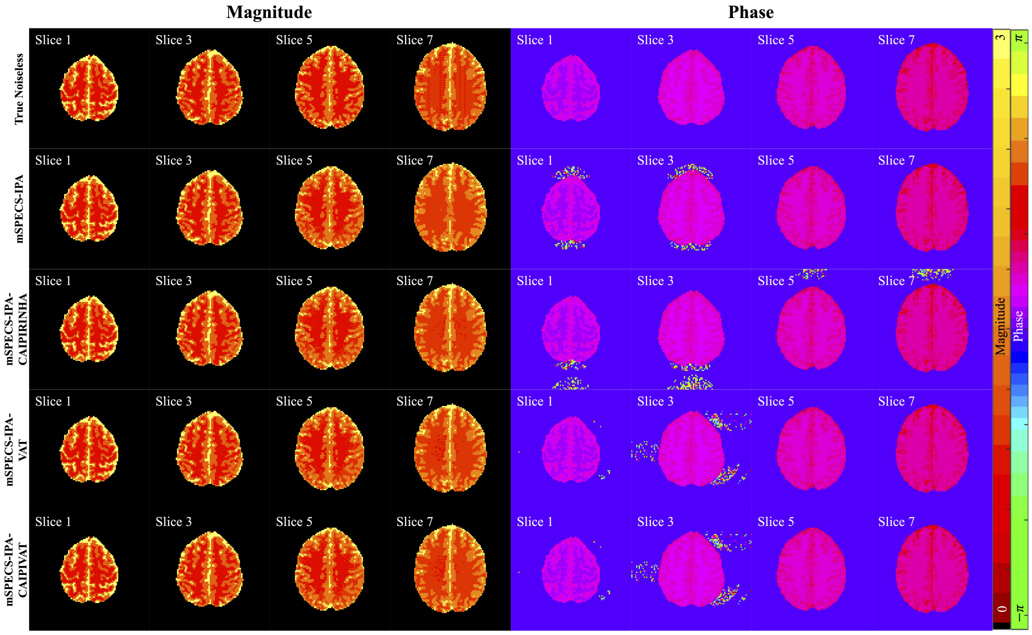

Figure 10: The magnitude and phase of the reconstructed images odd slices from mSPECS-IPA, mSPECS-IPA-CAIPIRINHA, mSPECS-IPA-VAT, and mSPECS-IPA-CAIPIVAT, compared with the magnitude and phase from true noiseless simulated images odd slices with TPA=2.

task images were artificially aliased from the fully acquired task time series, following a procedure similar to that used for generating simulated aliased task images. The artificially aliased task images for each model were primarily generated using different image shift techniques and 2D Hadamard encoding coefficients. The artificially aliased subsampled k-space data were obtained by skipping every other line in the fully sampled k-space of the summed images after applying the Fourier transform. The aliased task images were then reconstructed from the subsampled k-space using the inverse Fourier transform.

The last $N_{cal} = 40$ fully sampled non-task calibration images were used to assess the hyperparameter. The same acceleration factors from the simulated fMRI time series were applied in the real-world right-handed finger tapping experiment with $R = 2$, and $TPA = 2, 4, 8$. The same net acceleration factors were achieved in the real-world experimental time series. The mSPECS-IPA model, mSPECS-IPA-CAIPIRINHA model, mSPECS-IPA-VAT model and the mSPECS-IPA-CAIPIVAT model were applied to the right-handed

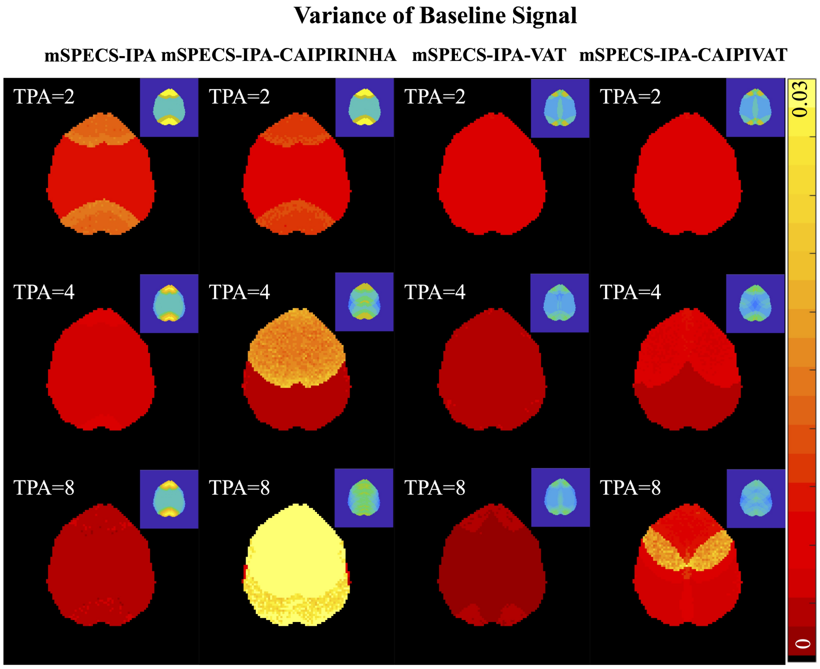

Figure 11: The variance of the baseline regression coefficient of slice 3 from reconstructed images from mSPECS-IPA, mSPECS-IPA-CAIPIRINHA, mSPECS-IPA-VAT, and mSPECS-IPA-CAIPIVAT model with different through-plane acceleration factors.

finger tapping experiment fMRI time series. The SENSE method was also applied to the calibration fMRI time series, and the reconstructed images were utilized as the reference images. The reconstructed results from the novel image shift SMS technique were compared with the reference images. All of the reconstruction and the analysis process were finished through the MATLAB programming software.

4. The Simulation Results

4.1. Non-Task Simulated Reconstruction Results

Based on the methodology of the novel proposed image shift SMS techniques, we conducted the simulated experiment with the same in-plane acceleration factor, $IPA = 2$, and different through-plane acceleration factors with $TPA = 2$, $TPA = 4$, and $TPA = 8$. The reconstructed results were compared between mSPECS-IPA model (without image shift technique), mSPECS-IPA-CAIPIRINHA model (image shift along vertical direc-

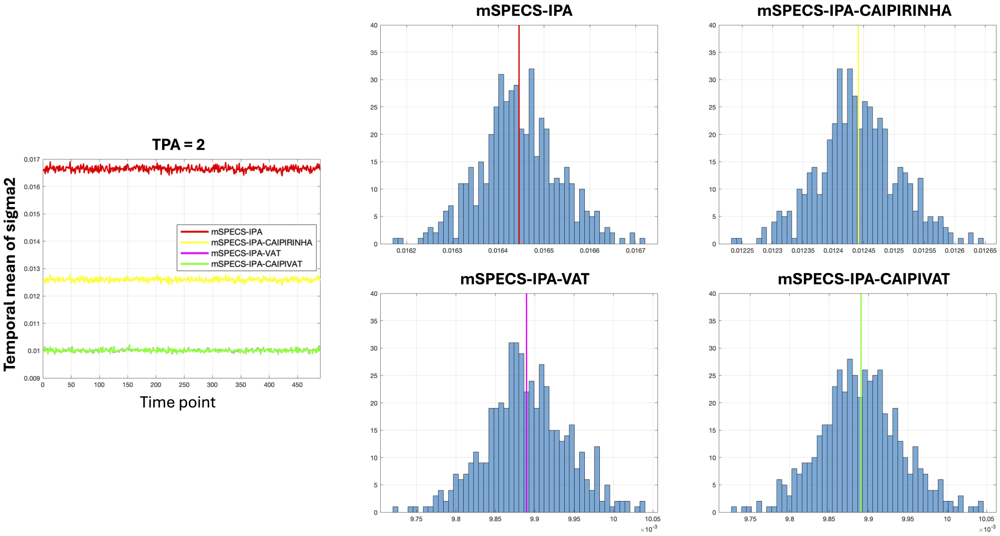

Figure 12: The temporal mean of residual variance of brain images reconstructed from mSPECS-IPA, mSPECS-IPA-CAIPIRINHA, mSPECS-IPA-VAT and mSPECS-IPA-CAIPIVAT model with IPA = 2 and TPA = 2.

tion), mSPECS-IPA-VAT model (image shift along horizontal direction), and mSPECS-IPA-CAIPIVAT (image shift along vertical and horizontal direction). The reconstructed results were also compared with the true noiseless simulated images. Fig. 10 shows the mean magnitude and mean phase from odd slices of the reconstructed images from mSPECS-IPA, mSPECS-IPA-CAIPIRINHA, mSPECS-IPA-VAT, and mSPECS-IPA-CAIPIVAT, compared with the magnitude and phase from true noiseless simulated images, and the through-plane acceleration factor is 2. Fig. 10 is generated based on Eq. 24. Compared to the true magnitude, the mean magnitude from these four models is closely aligned with the true value. No inter-slice signal leakage or artifact distortions appear in the mean magnitude images. The mean phase of the reconstructed images from these four models is also consistent with the phase value of the true noiseless simulated image inside the brain. However, residuals are present outside the brain in the mSPECS-IPA, mSPECS-IPA-CAIPIRINHA, mSPECS-IPA-VAT, and mSPECS-IPA-CAIPIVAT models due to differences in the image shift techniques and slice overlapping conditions in each model. Fig. 11 was generated according to Eq. 25. The top-right corner displays the overlapping indicator for each novel SMS image reconstruction model, incorporating different TPA factors. It represents

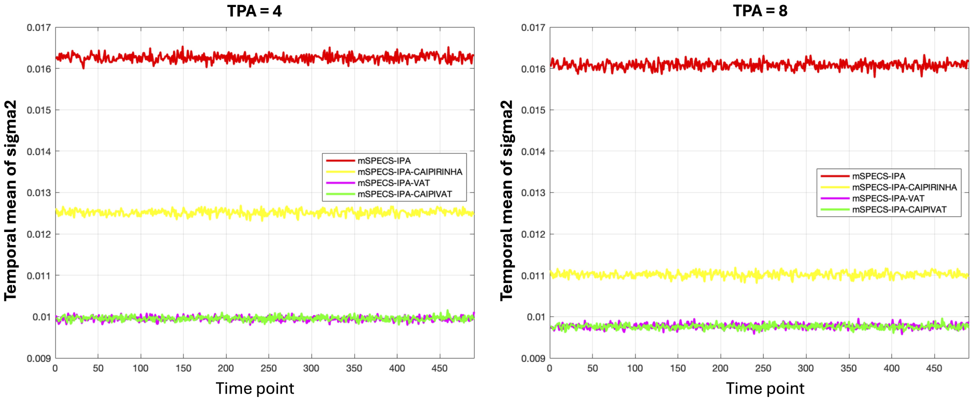

Figure 13: The temporal mean of residual variance of brain images reconstructed from mSPECS-IPA, mSPECS-IPA-CAIPIRINHA, mSPECS-IPA-VAT and mSPECS-IPA-CAIPIVAT model with IPA = 2 and TPA = 4 and 8.

the slice overlapping and voxel aliasing situation for each approach and acceleration factor. When the acceleration factor is low, IPA = 2 and TPA = 2, all four models have a low variance at the center of the brain image. However, due to a high overlapping indicator value at the anterior and posterior regions, high variance is detected at these region. As the acceleration factor increases, models that do not incorporating with vertical image shift technique, mSPECS-IPA and mSPECS-IPA-VAT model, show a decrease in task regression coefficient variance. On the other hand, models that incorporate with the vertical image shift technique, mSPECS-IPA-CAIPIRINHA and mSPECS-IPA-CAIPIVAT model, exhibit an increase in task regression coefficient variance in the anterior region of the brain image. Among these four models, the mSPECS-IPA-CAIPIRINHA has the highest task regression coefficient variance when IPA = 2 and TPA = 8. The temporal variance of the task signal is shown in the Appendix A Fig. A.21.

Fig. 12 displays temporal mean of residual variance of brain images reconstructed from mSPECS-IPA, mSPECS-IPA-CAIPIRINHA, mSPECS-IPA-VAT and mSPECS-IPA-CAIPIVAT model with IPA = 2 and TPA = 2. Fig. 13 shows temporal mean of residual variance for brain images reconstructed from same models but with acceleration factors IPA = 2 and TPA = 4 and 8. Fig. 12 and Fig. 13 are generated based on Eq. 27. For each acceleration factor, among the four models, mSPECS-IPA has the highest temporal mean of residual variance, whereas the models incorporating the horizontal image shift technique, mSPECS-IPA-VAT and mSPECS-IPA-CAIPIVAT, exhibit the lowest temporal mean of residual variance. As the acceleration factor increases, the temporal mean of residual variance slightly decreases across all four models. We also investigated the temporal variance of the residual variance of brain images reconstructed from mSPECS-IPA, mSPECS-IPA-CAIPIRINHA, mSPECS-IPA-VAT and mSPECS-IPA-CAIPIVAT model with IPA = 2 and TPA = 2, 4, and 8, which is shown in Appendix A Fig. A.22 and Fig. A.23.

We also investigated the signal-to-noise ratio (*SNR*) and the geometric factor g-factor values across mSPECS-IPA, mSPECS-IPA-CAIPIRINHA, mSPECS-IPA-VAT, and mSPECS-IPA-CAIPIVAT models. The *SNR* can be calculated as $SNR = \beta_0/\sigma_N$, where β_0 represents the baseline signal for each location of the brain image, and σ_N represents the standard deviation of the noise. The higher the *SNR* value is, the better performance of the model. According to the definition of g-factor (Eq. 1) in Section 2.1.1, the through-plane acceleration factor also need to be incorporated into it. Thus, the g-factor can be calculated as $g_{accelerate} = \sqrt{N_s} SNR_{full}/SNR_{accelerate}\sqrt{R}$, where $R = 2$ indicating the in-plane acceleration factor. The closer g-factor is to 1, the better reconstructed results the model will produce. Fig. 14A shows the *SNR* value of slice 3 for four models with different through-plane acceleration factors. The top right corner is the slice overlapping situation corresponding to average of the first N_α time point for each model. As the TPA factor increases, the *SNR* value for the mSPECS-IPA and mSPECS-IPA-VAT models also increases. Moreover, in the mSPECS-IPA-VAT model, both the posterior and anterior regions of the brain exhibit higher *SNR* values compared to the mSPECS-IPA model. In contrast, for the mSPECS-IPA-CAIPIRINHA and mSPECS-IPA-CAIPIVAT models, the *SNR* value does not increase evenly across the entire brain image as the TPA factor increases. In the mSPECS-IPA-CAIPIRINHA model, at higher TPA factors, the *SNR* in the middle brain region is lower than at lower TPA factors. A similar pattern is observed in the left side of the brain image in the mSPECS-IPA-CAIPIVAT model. Fig. 14B shows the g-factor of slice 3 across different models with varying through-plane acceleration factors. As the TPA factor increases, the g-factor in the mSPECS-IPA-CAIPIRINHA and mSPECS-IPA-CAIPIVAT models increases dramatically, whereas in the mSPECS-IPA and mSPECS-IPA-VAT models, it increases only slightly. Comparing the g-factor values between the mSPECS-IPA and mSPECS-IPA-VAT models, the g-factor in the mSPECS-IPA-VAT model is closer to 1 in both the posterior

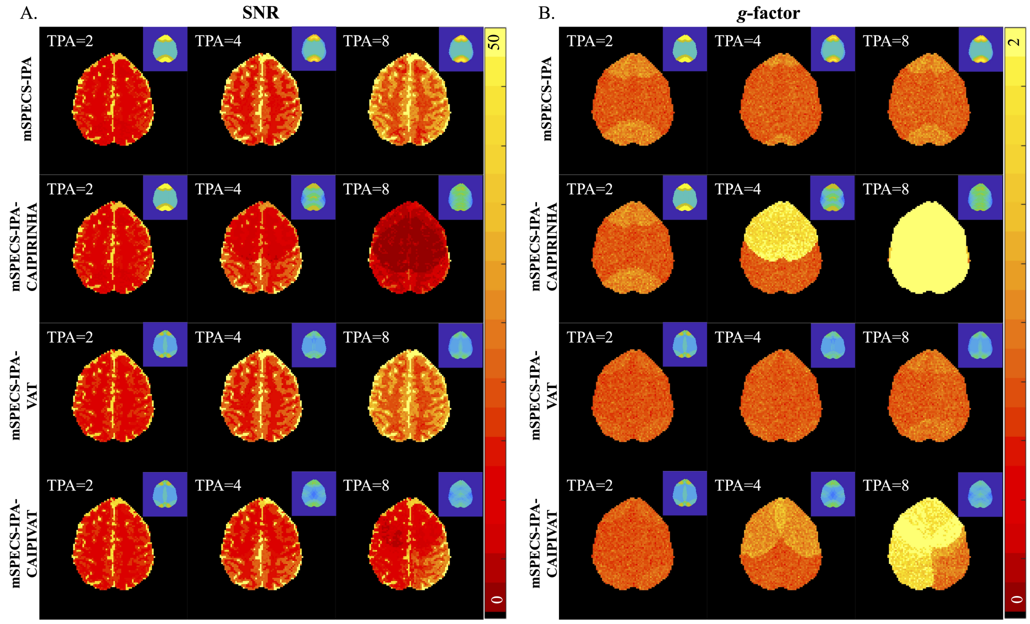

Figure 14: A. The *SNR* value of slice 3 from reconstructed images for mSPECS-IPA, mSPECS-IPA-CAIPIRINHA, mSPECS-IPA-VAT, and mSPECS-IPA-CAIPIVAT model with different TPA factor. B. The g-factor value of slice 3 from reconstucted images for mSPECS-IPA, mSPECS-IPA-CAIPIRINHA, mSPECS-IPA-VAT, and mSPECS-IPA-CAIPIVAT model with different TPA factor.

and anterior regions of the brain. The anterior artifacts observed at higher acceleration factors are consistent with insufficient coil sensitivity diversity rather than failure of the reconstruction framework itself. These artifacts are expected under aggressive SMS acceleration when using low channel count receiver coils.

4.2. Task Simulated Reconstruction Results

In order to investigate the task activation detection performance of each model, we applied the novel image shift SMS techniques to the simulated right-handed finger tapping experiment with the same in-plane acceleration factor, IPA=2, and different through-plane acceleration factors TPA=2, TPA=4, and TPA=8. For each voxel in the brain image, the signal can be expressed as $y = \beta_0 + \beta_1 x + \epsilon$, where β_0 is the baseline signal of the voxel, β_1 is the task signal, x is a vector with elements 0 and 1 indicating each time point with or without task activation. Therefore, the contrast-to-noise ratio (*CNR*)

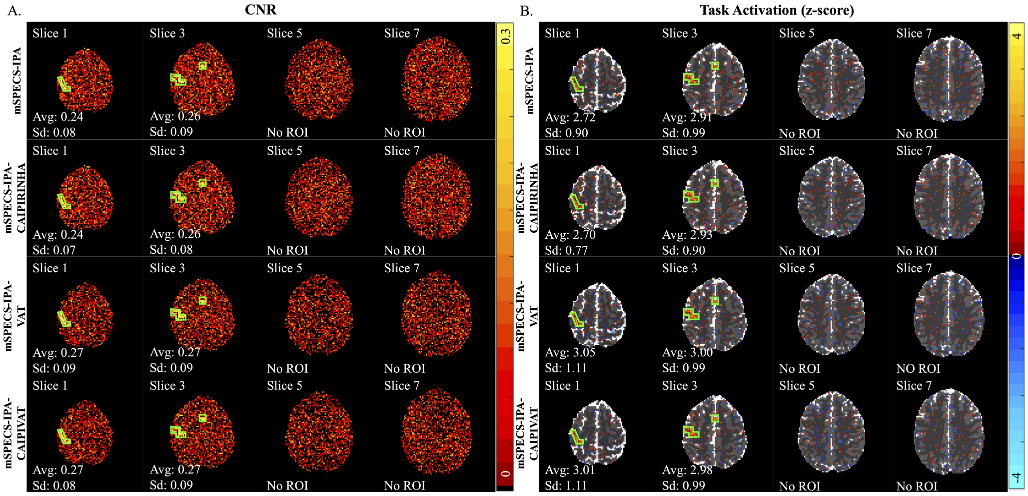

Figure 15: A. The average *CNR* value of ROI for odd slices with acceleration factor TPA=2 from mSPECS-IPA, mSPECS-IPA-CAIPIRINHA, mSPECS-IPA-VAT, and mSPECS-IPA-CAIPIVAT model. B. The average task activation rate (z-score) of ROI for odd slices with acceleration factor TPA=2 from mSPECS-IPA, mSPECS-IPA-CAIPIRINHA, mSPECS-IPA-VAT, and mSPECS-IPA-CAIPIVAT model.

can be calculated as $CNR = \beta_1/\sigma_N$, and same as the definition in *SNR*, σ_N stands for the standard deviation of the noise. The activation detection rate for each model was also investigated by applying a complex-valued model to compute fMRI activation (Rowe and Logan [18]). Fig. 15A shows the average and standard deviation of the *CNR* values in the region of interest (ROI) for odd slices from the mSPECS-IPA, mSPECS-IPA-CAIPIRINHA, mSPECS-IPA-VAT, and mSPECS-IPA-CAIPIVAT models with an acceleration factor of TPA = 2. The *CNR* value of the ROI for slice 1 in the mSPECS-IPA-VAT and mSPECS-IPA-CAIPIVAT models is slightly higher than in the mSPECS-IPA and mSPECS-IPA-CAIPIRINHA models. Meanwhile, the *CNR* value of the ROI for slice 3 is similar across all four models. Fig. 15B shows the average task activation detection rate in the ROI for odd slices from the mSPECS-IPA, mSPECS-IPA-CAIPIRINHA, mSPECS-IPA-VAT, and mSPECS-IPA-CAIPIVAT models with TPA = 2. Compared to the models with a horizontal image shift, mSPECS-IPA-VAT and mSPECS-IPA-CAIPIVAT, the models without horizontal image shift, mSPECS-IPA and mSPECS-IPA-CAIPIRINHA, exhibit a lower average z-score in the ROI. This indicates that the activation detection ability of mSPECS-IPA and

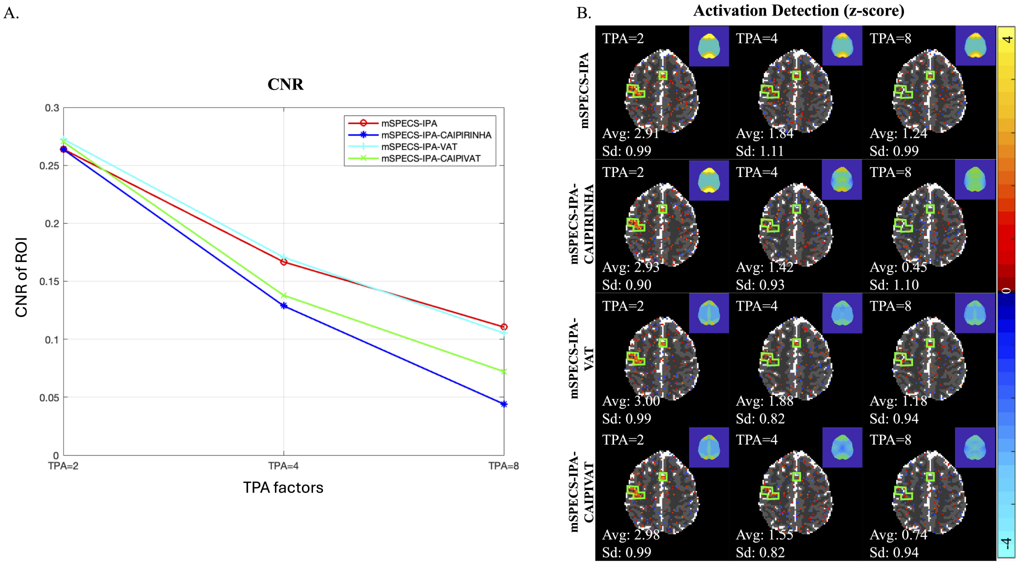

Figure 16: A. The average *CNR* value of ROI for slice 3 from mSPECS-IPA, mSPECS-IPA-CAIPIRINHA, mSPECS-IPA-VAT, and mSPECS-IPA-CAIPIVAT model with acceleration factor TPA=2, TPA=4, and TPA=8. B. The average activation detection rate (z-score) of ROI for slice 3 from mSPECS-IPA, mSPECS-IPA-CAIPIRINHA, mSPECS-IPA-VAT, and mSPECS-IPA-CAIPIVAT model with acceleration factor TPA=2, TPA=4, and TPA=8.

mSPECS-IPA-CAIPIRINHA is lower than that of the mSPECS-IPA-VAT and mSPECS-IPA-CAIPIVAT models.

To assess the influence of a high acceleration factor on the task activation detection ability of each model, we compared the *CNR* value and the task activation detection rate of ROI for mSPECS-IPA, mSPECS-IPA-CAIPIRINHA, mSPECS-IPA-VAT, and mSPECS-IPA-CAIPIVAT models under different acceleration factors, TPA = 2, TPA = 4, and TPA = 8. Fig. 16A shows the average *CNR* value in the ROI of slice 3 for the mSPECS-IPA, mSPECS-IPA-CAIPIRINHA, mSPECS-IPA-VAT, and mSPECS-IPA-CAIPIVAT models with different acceleration factors. As the acceleration factor increases, the average *CNR* value decreases across all four models. However, at high acceleration factors, the average *CNR* value in the ROI is higher in the mSPECS-IPA and mSPECS-IPA-VAT models compared to the models incorporating vertical image shift, mSPECS-IPA-CAIPIRINHA and mSPECS-IPA-CAIPIVAT. Among these models, the model applies image shift only along the vertical direction, mSPECS-IPA-CAIPIRINHA exhibits the lowest average *CNR* value in the ROI. Fig. 16B shows the activation detection rate (z-score) in the ROI of slice 3 for the mSPECS-IPA, mSPECS-IPA-CAIPIRINHA, mSPECS-IPA-VAT, and mSPECS-IPA-CAIPIVAT models with different acceleration factors. As the acceleration factor increases, it becomes more difficult to capture the entire simulated activation blocks across all four models. However, at TPA = 8, the models without vertical image shift, mSPECS-IPA and mSPECS-IPA-VAT, exhibit higher average z-scores in the ROI compared to the models with vertical image shift, mSPECS-IPA-CAIPIRINHA and mSPECS-IPA-CAIPIVAT. Although the models incorporating vertical image shift exhibit lower average z-scores in the ROI, the mSPECS-IPA-CAIPIVAT model achieves a higher average z-score compared to the mSPECS-IPA-CAIPIRINHA model. Among all models, mSPECS-IPA-CAIPIRINHA provides the lowest activation detection rate, indicating that it has the least ability to capture the simulated task activation blocks. Although the proposed method exhibits higher mean *CNR* and activation detection rates across several configurations, the associated variability indicates that these improvements are not uniformly statistically significant. These findings suggest potential benefits that depend on acquisition parameters, encoding strategy, and brain region, rather than a guaranteed performance improvement in all settings.

5. The Experimental Results

5.1. Non-Task Experimental Reconstruction Results

To investigate the performance of the proposed novel image-shifted SMS techniques in a real-world fMRI experiment, we applied four models to an in vivo right-handed finger-tapping fMRI time series. The reconstruction results from these models were compared with reference axial brain images, reconstructed using the SENSE technique from the calibration axial brain image time series. Additionally, we applied the novel image-shifted SMS techniques with the same in-plane acceleration factor, IPA = 2, and varying through-plane acceleration factors, TPA = 2, TPA = 4, and TPA = 8, to examine the impact of acceleration on each model. Fig. 17 shows the mean magnitude and mean phase of the odd slices reconstructed with TPA = 2 from the mSPECS-IPA, mSPECS-IPA-CAIPIRINHA, mSPECS-IPA-VAT, and mSPECS-IPA-CAIPIVAT models, compared to the mean magnitude and mean phase of the reference image from the calibration images. Compared to the mean magnitude of the reference image, the mean magnitude from

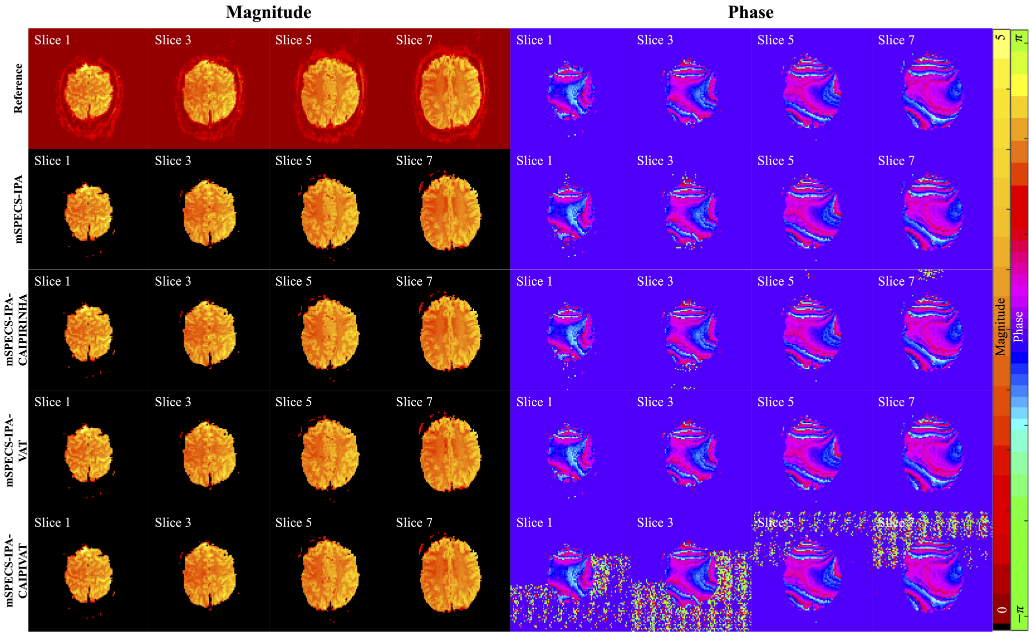

Figure 17: The mean magnitude and mean phase of the odd slices from reconstructed image with through-plane acceleration factor TPA=2 corresponding to mSPECS-IPA, mSPECS-IPA-CAIPIRINHA, mSPECS-IPA-VAT and mSPECS-IPA-CAIPIVAT model.

the four image-shifted SMS models is closely aligned with the reference image. No inter-slice signal leakage or artifactual brain distortions from other slices were observed in the reconstructed images. Compared to the mean phase of the reference image, the mean phase of the reconstructed images from the mSPECS-IPA, mSPECS-IPA-CAIPIRINHA, mSPECS-IPA-VAT, and mSPECS-IPA-CAIPIVAT models exhibits a highly similar pattern inside the brain. However, residual artifacts appear outside the brain, particularly in the mSPECS-IPA-CAIPIRINHA and mSPECS-IPA-CAIPIVAT models, which can be attributed to voxel aliasing, slice overlapping, and image shift techniques applied in different models. The temporal variance of the task signal is shown in Appendix B Fig. A.24.

Similar to the simulation-based reconstructed axial brain image analysis, we also investigate the signal-to-noise ratio (SNR) and the geometric factor (g-factor) in the reconstructed brain images from the mSPECS-IPA, mSPECS-IPA-CAIPIRINHA, mSPECS-IPA-VAT, and mSPECS-IPA-CAIPIVAT models under different acceleration factors. The SNR value and

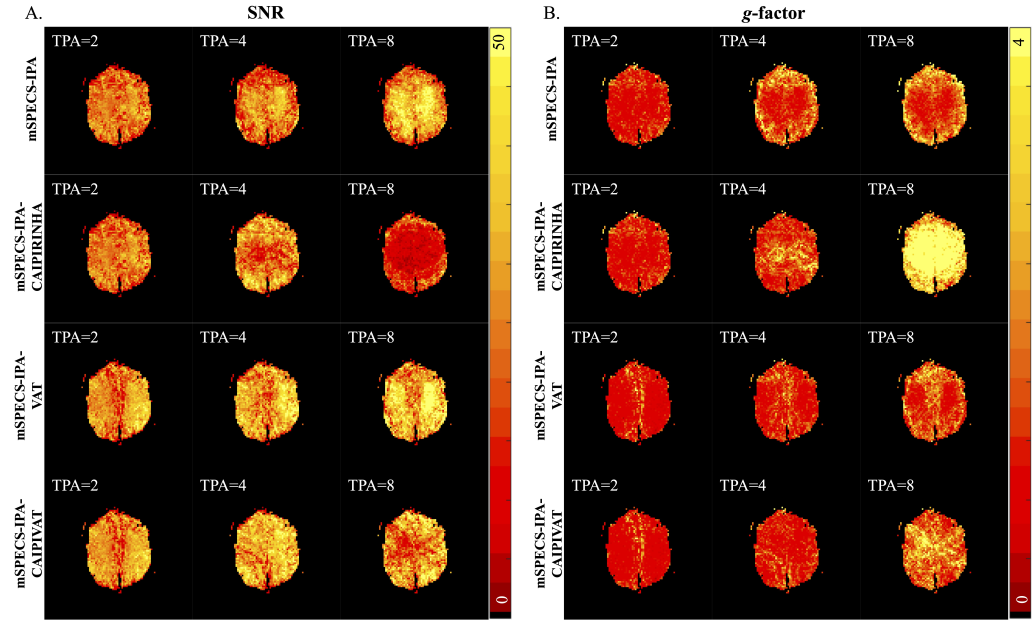

Figure 18: A. The *SNR* value of reconstructed brain images slice 3 from mSPECS-IPA, mSPECS-IPA-CAIPIRINHA, mSPECS-IPA-VAT and mSPECS-IPA-CAIPIVAT model with different acceleration factors. B. The g-factor value of reconstructed brain images slice 3 from mSPECS-IPA, mSPECS-IPA-CAIPIRINHA, mSPECS-IPA-VAT and mSPECS-IPA-CAIPIVAT model with different acceleration factors.

the g-factor are calculated as described in Section 4.1. Fig. 18A shows the average *SNR* value for slice 3 in the mSPECS-IPA, mSPECS-IPA-CAIPIRINHA, mSPECS-IPA-VAT, and mSPECS-IPA-CAIPIVAT models with acceleration factors TPA $= 2$, TPA $= 4$, and TPA $= 8$. As the acceleration factor increases, the average *SNR* in the mSPECS-IPA and mSPECS-IPA-VAT models also increases. The mSPECS-IPA-VAT model exhibits a higher average *SNR* at the edges of the brain image compared to the mSPECS-IPA model. Conversely, in the models incorporating vertical image shift (mSPECS-IPA-CAIPIRINHA and mSPECS-IPA-CAIPIVAT), the average *SNR* initially increases as the acceleration factor increases from TPA $= 2$ to TPA $= 4$ but decreases at TPA $= 8$. Comparing the average *SNR* of the reconstructed axial brain images across the four models, the mSPECS-IPA-VAT model provides the highest *SNR* value. Fig. 18B shows the g-factor of the reconstructed image of slice 3 for the mSPECS-IPA, mSPECS-IPA-CAIPIRINHA, mSPECS-IPA-VAT, and mSPECS-IPA-CAIPIVAT models under different acceleration factors. Although the g-factor increases across all four models as the acceleration factor increases, the mSPECS-IPA-VAT model exhibits the lowest g-factor compared to the other three models. In contrast, the mSPECS-IPA-CAIPIRINHA model has the highest g-factor among the four models at TPA = 8.

5.2. Task Experimental Reconstruction Results

To analyze the activation detection ability of the proposed image-shifted SMS technique in a real-world right-handed finger-tapping fMRI experiment, we also investigate the contrast-to-noise ratio (CNR) and the activation detection rate (z-score) of ROI of the reconstructed axial brain images from the mSPECS-IPA, mSPECS-IPA-CAIPIRINHA, mSPECS-IPA-VAT, and mSPECS-IPA-CAIPIVAT models under different acceleration factors. Since the right-handed finger-tapping fMRI experiment was conducted, the task activation area was expected to be in the left motor cortex of the brain. Fig. 19A shows the average CNR value in the ROI for odd slices of the reconstructed images from the mSPECS-IPA, mSPECS-IPA-CAIPIRINHA, mSPECS-IPA-VAT, and mSPECS-IPA-CAIPIVAT models with an acceleration factor of TPA = 2. Compared to models without horizontal image shift, mSPECS-IPA and mSPECS-IPA-CAIPIRINHA, models incorporating horizontal image shift, mSPECS-IPA-VAT and mSPECS-IPA-CAIPIVAT, exhibit a higher average CNR value in the ROI, with mSPECS-IPA-VAT achieving the highest CNR value among the four models. Fig. 19B shows the task activation detection rate for odd slices of the reconstructed images from the mSPECS-IPA, mSPECS-IPA-CAIPIRINHA, mSPECS-IPA-VAT, and mSPECS-IPA-CAIPIVAT models with TPA = 2. Similar to the conclusion drawn from the average CNR in the ROI, the mSPECS-IPA-VAT and mSPECS-IPA-CAIPIVAT models exhibit a higher average z-score in the ROI of the left motor cortex compared to the mSPECS-IPA and mSPECS-IPA-CAIPIRINHA models. Among these four models, the mSPECS-IPA-VAT model provides the best activation detection map at TPA = 2, indicating that mSPECS-IPA-VAT is the most sensitive model for detecting task activation blocks.

The average CNR value in the ROI and the task activation detection rate were also analyzed for the mSPECS-IPA, mSPECS-IPA-CAIPIRINHA, mSPECS-IPA-VAT, and mSPECS-IPA-CAIPIVAT models under different acceleration factors. Fig. 20A shows the average CNR value in the ROI of slice 3 for the four models, compared at different acceleration factors,

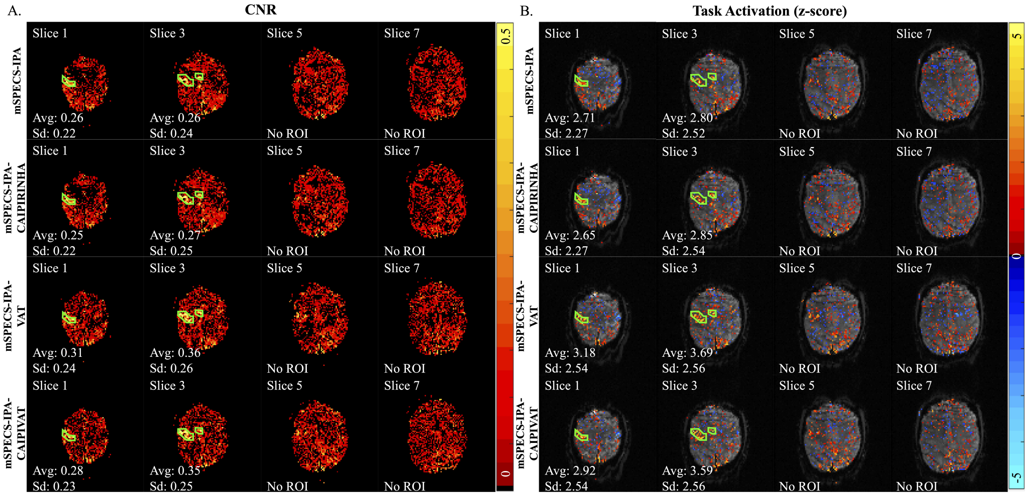

Figure 19: A. The average *CNR* value of ROI for odd slices of reconstructed images from mSPECS-IPA, mSPECS-IPA-CAIPIRINHA, mSPECS-IPA-VAT and mSPECS-IPA-CAIPIVAT model with TPA=2. B. The task activation detection (z-score) map of ROI for odd slices of reconstructed images from mSPECS-IPA, mSPECS-IPA-CAIPIRINHA, mSPECS-IPA-VAT and mSPECS-IPA-CAIPIVAT model with TPA=2.

TPA = 2, TPA = 4, and TPA = 8. As the acceleration factor increases, the average *CNR* decreases significantly across all four models. However, among them, the mSPECS-IPA-VAT model provides the highest average *CNR* in the ROI, while the mSPECS-IPA-CAIPIRINHA model exhibits the lowest average *CNR*. Moreover, models incorporating horizontal image shift exhibit a higher average *CNR* in the ROI compared to models without horizontal image shift. Fig. 20B shows the average task activation detection map for the ROI of slice 3 across the four models with different acceleration factors. As the acceleration factor increases, the average z-score in the ROI decreases significantly for each model. Among these four models, the mSPECS-IPA-VAT model provides the highest average z-score in the ROI, while the mSPECS-IPA-CAIPIRINHA model exhibits the lowest. Additionally, models incorporating vertical image shift exhibit a lower average z-score compared to models without vertical image shift. The mSPECS-IPA-VAT model demonstrates the strongest ability to detect task activation blocks in brain images.

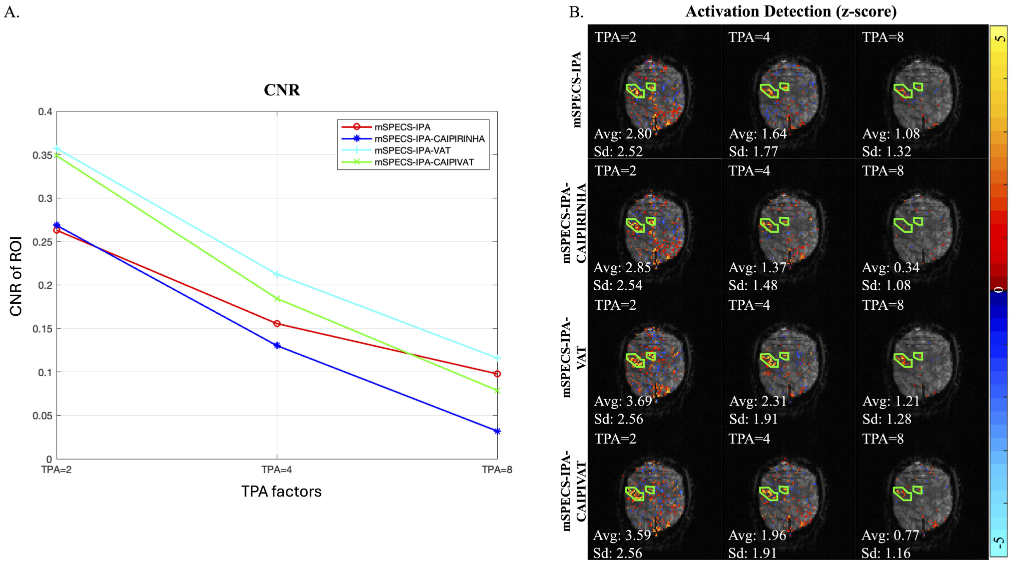

Figure 20: A. The average *CNR* value of ROI for slice 3 from mSPECS-IPA, mSPECS-IPA-CAIPIRINHA, mSPECS-IPA-VAT, and mSPECS-IPA-CAIPIVAT model with acceleration factor TPA=2, TPA=4, and TPA=8. B. The average activation detection rate (z-score) of ROI for slice 3 from mSPECS-IPA, mSPECS-IPA-CAIPIRINHA, mSPECS-IPA-VAT, and mSPECS-IPA-CAIPIVAT model with acceleration factor TPA=2, TPA=4, and TPA=8.

6. Discussion

In traditional fMRI image acquisition techniques, images were collected slice-by-slice during the early development of fMRI studies. As imaging techniques advanced, researchers focused on improving the efficiency of the image acquisition process while maintaining the ability to reconstruct high-resolution brain images. Two primary techniques have been developed to achieve this goal: through-plane acceleration and in-plane acceleration. Parallel imaging is one of the through-plane acceleration techniques, allowing multiple brain images to be acquired at each time point in an fMRI time series. Previous studies suggest that an optimal multiband factor for resting-state fMRI is MB $= 4$ (Risk et al. [16]). A widely used in-plane acceleration technique, GRAPPA, can also reduce scan time by acquiring a subsampled k-space. In this study, through-plane acceleration and in-plane acceleration were combined to further shorten image scan time. However, due to the high similarity of coil sensitivity information in aliased voxels, additional techniques such as 2D Hadamard phase encoding and image shift were incorporated to mitigate the influence of the g-factor. As discussed in Section 2.1.2, the number of aliased brain images should be a power of 2 due to the constraints of the 2D Hadamard coefficient aliasing matrix. However, if an odd number of images are aliased, the orthogonal contrast aliasing matrix design can be incorporated into the model to maintain the orthogonality of the design matrix. In this study, we not only investigated the influence of net acceleration factors and image shift directions on model performance but also assessed the task activation detection ability of each model. The proposed 2D Hadamard encoded SMS framework requires multiple excitations to separate aliased slices, effectively reducing the temporal sampling rate compared to conventional single-shot SMS acquisitions. As a result, this approach is not intended to replace ultra fast SMS protocols designed for high temporal resolution event-related fMRI. Instead, it is best suited for block design or moderate TR paradigms where improved encoding diversity, reduced slice leakage, and enhanced CNR characteristics may outweigh the reduction in temporal resolution.

In this study, we first investigated the influence of high acceleration factors on the performance of the mSPECS-IPA, mSPECS-IPA-CAIPIRINHA, mSPECS-IPA-VAT, and mSPECS-IPA-CAIPIVAT models. Based on the simulated reconstructed results in Section 4 and the experimentally reconstructed results in Section 5, high acceleration factors had a positive impact on the SNR of the reconstructed images in the mSPECS-IPA and mSPECS-IPA-VAT models. As shown in Fig. 14 and Fig. 18, as the acceleration factor increased, the average SNR also increased. However, in models incorporating vertical image shift, the SNR of the reconstructed images decreased as the acceleration factor increased. This effect occurs because image shift in the same direction as the in-plane acceleration results in a more complex slice-overlapping pattern than in models without vertical image shift. A similar conclusion can be drawn from the g-factor plot. The g-factor penalty in the mSPECS-IPA and mSPECS-IPA-VAT models is more stable compared to the mSPECS-IPA-CAIPIRINHA and mSPECS-IPA-CAIPIVAT models. As shown in Fig. 16 and Fig. 20, a high acceleration factor negatively affects the average CNR in each model. As the acceleration factor increased, the average CNR in the ROI decreased significantly across all models. However, among the four models, the mSPECS-IPA-VAT model exhibited the highest average CNR across different acceleration factors. A similar trend was observed in the task activation detection maps for each model under different acceleration factors. As the acceleration factor increased, the average z-score in the ROI decreased, indicating that capturing task activation signals became more difficult for all models at high acceleration factors. However, the mSPECS-IPA-VAT model maintained the highest average z-score in the ROI, making it the most sensitive model for detecting activation signals compared to the other models. Thus, with increasing through-plane acceleration, the *SNR* increases for all models, but the *CNR* values and task activation detection rates decrease. This trade-off necessitates a careful choice of the acceleration factor. Moreover, to balance the activation detection rate with efficient image acquisition, the recommended acceleration factors are TPA = 2 and IPA = 2.

We also investigated the influence of the image shift direction on the performance of each model. There are four different directions: mSPECS-IPA has no image shift technique, mSPECS-IPA-CAIPIRINHA has vertical image shift technique, mSPECS-IPA-VAT has horizontal image shift technique and the mSPECS-IPA-CAIPIVAT has vertical and horizontal image shift technique. Comparing the *SNR*, average *CNR* plot, and task activation detection maps, models incorporating vertical image shift, mSPECS-IPA-CAIPIRINHA and mSPECS-IPA-CAIPIVAT exhibited worse results in the reconstructed brain images. This is due to the increased voxel aliasing complexity when image shift occurs in the same direction as the in-plane acceleration (i.e., the phase encoding direction). Therefore, to avoid degraded reconstruction performance, it is recommended that image shift be applied in a direction different from the in-plane acceleration direction.

Moreover, other factors may also influence the performance of the novel image shift SMS technique, such as the location of the task activation signal and the size of the brain image. For example, if the task activation signal is generated in the posterior or anterior region of the brain, the mSPECS-IPA-VAT model is expected to perform better than the other models. In conclusion, the novel image-shifted SMS technique is recommended to be used with a lower acceleration factor, and the image shift direction should be different from the in-plane acceleration direction to achieve optimal performance. The proposed Bayesian reconstruction framework is not designed as a direct replacement for Slice-GRAPPA or Split Slice-GRAPPA in standard SMS acquisitions. Rather, it offers an alternative modeling perspective that emphasizes probabilistic inference, explicit uncertainty quantification, and the interaction between image shift strategies and encoding diversity. Future work will include direct comparisons using true multiband acquisitions with

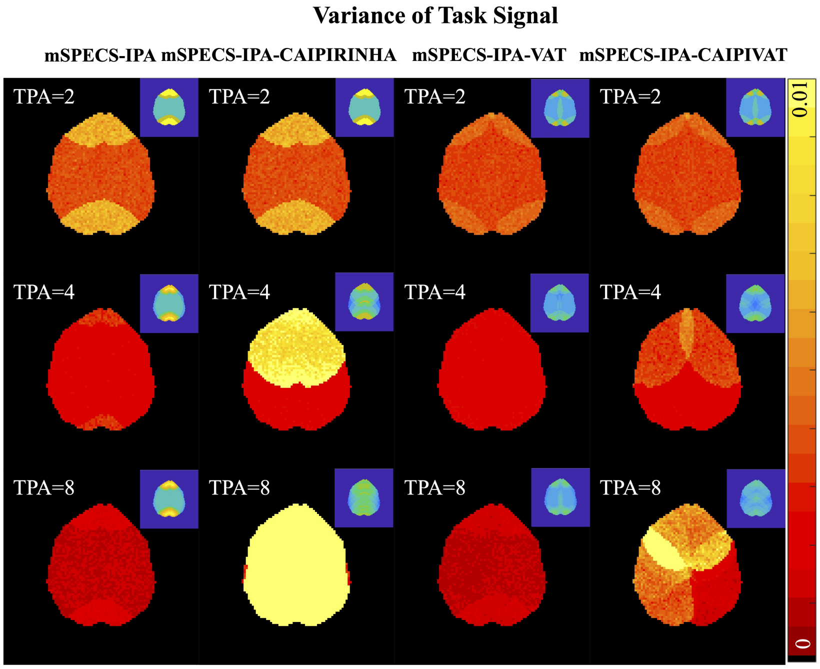

Figure A.21: The task regression coefficient variance of slices 3 from reconstructed images from mSPECS-IPA, mSPECS-IPA-CAIPIRINHA, mSPECS-IPA-VAT, and mSPECS-IPA-CAIPIVAT model with different through-plane acceleration factors.

high channel count receiver arrays.

7. Acknowledgment

The authors thank the Wehr Foundation as this research is funded by the Computational Sciences Summer Research Fellowship (CSSRF) at Marquette University in the Department of Mathematical and Statistical Sciences. *Conflict of Interest*: None declared.

Appendix A. Supplemental Simulation Results

In the main text, we displays the temporal variance of the baseline signal of slice 3 from reconstructed images corresponding to four SMS models: mSPECS-IPA, mSPECS-IPA-CAIPIRINHA, mSPECS-IPA-VAT, and mSPECS-IPA-CAIPIVAT model with different through-plane acceleration factors. Fig. A.21 shows the temporal variance of task coefficient of slice 3

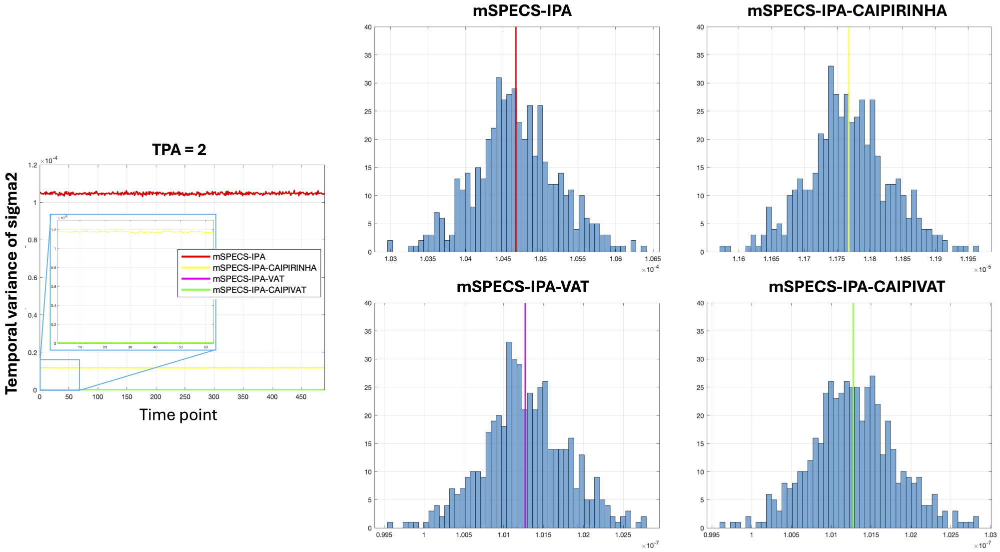

Figure A.22: The variance of the baseline regression coefficient of slice 3 from reconstructed images from mSPECS-IPA, mSPECS-IPA-CAIPIRINHA, mSPECS-IPA-VAT, and mSPECS-IPA-CAIPIVAT model with different through-plane acceleration factors.

from the reconstructed images corresponding to the mSPECS-IPA, mSPECS-IPA-CAIPIRINHA, mSPECS-IPA-VAT, and mSPECS-IPA-CAIPIVAT with different through-plane acceleration factors. The top right corner is the slice

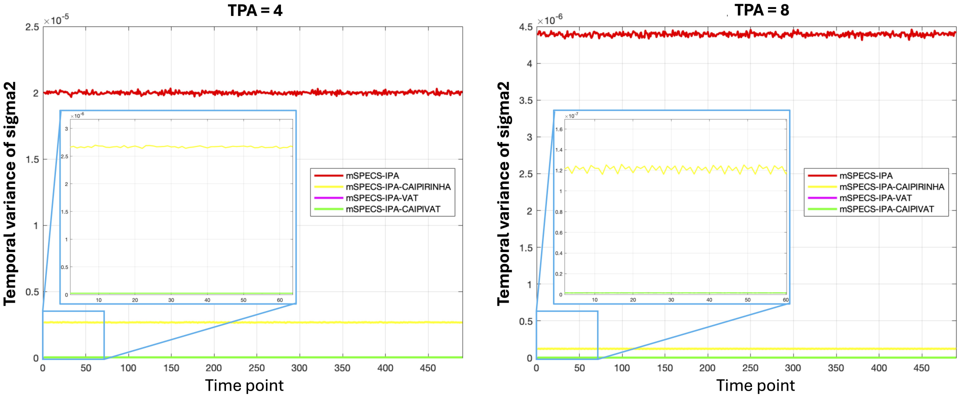

Figure A.23: The variance of the baseline regression coefficient of slice 3 from reconstructed images from mSPECS-IPA, mSPECS-IPA-CAIPIRINHA, mSPECS-IPA-VAT, and mSPECS-IPA-CAIPIVAT model with different through-plane acceleration factors.

overlapping situation corresponding to the average of first N_α time point for each model, indicating the voxel aliasing complexity for each method. For TPA = 2 and IPA = 2, the voxel aliasing and slice overlapping conditions are identical for the mSPECS-IPA and mSPECS-IPA-CAIPIRINHA models, as well as for the mSPECS-IPA-VAT and mSPECS-IPA-CAIPIVAT models. Consequently, the temporal variance of the reconstructed images from mSPECS-IPA is similar to that of mSPECS-IPA-CAIPIRINHA, while mSPECS-IPA-VAT exhibits similar behavior to mSPECS-IPA-CAIPIVAT. Comparing temporal variance across different models, mSPECS-IPA and mSPECS-IPA-CAIPIRINHA yield higher variance values than mSPECS-IPA-VAT and mSPECS-IPA-CAIPIVAT, particularly in the posterior-to-anterior regions of the brain. When the through-plane acceleration factor increases to 4 and 8, mSPECS-IPA-CAIPIRINHA exhibits the highest temporal variance among the four models. Although the temporal variance in the posterior region is lower for mSPECS-IPA-CAIPIVAT compared to mSPECS-IPA-CAIPIRINHA, high temporal variance values are observed in the anterior region of the brain in the mSPECS-IPA-CAIPIVAT model. The mSPECS-IPA and mSPECS-IPA-VAT demonstrate better temporal variance performance compared to models incorporating vertical shifts. Among the four models, mSPECS-IPA-VAT provides the best temporal variance performance at high acceleration factors.

Fig. A.22 shows the temporal variance of the residual variance for brain images reconstructed from four SMS models: mSPECS-IPA, mSPECS-IPA-CAIPIRINHA, mSPECS-IPA-VAT and mSPECS-IPA-CAIPIVAT model with IPA = 2 and TPA = 2. Fig. A.23 shows the temporal variance of the residual variance for brain images reconstructed from the same model but with acceleration factor IPA = 2 and TPA = 4 and 8. Fig. A.22 and Fig. A.23 are generated from Eq. 28. For each acceleration factor, the mSPECS-IPA model has the highest temporal variance of residual variance, while the mSPECS-IPA-VAT and mSPECS-IPA-CAIPIVAT models have the lowest, with values approaching zero. Moreover, as the acceleration factor increases, the temporal variance of residual variance decreases for all four models.

Appendix B. Supplemental Experimental Results

Fig. A.24 shows the temporal variance of the reconstructed image of slice 3 for each model under different acceleration factors. As the acceleration factor increases, the temporal variance increases significantly in the

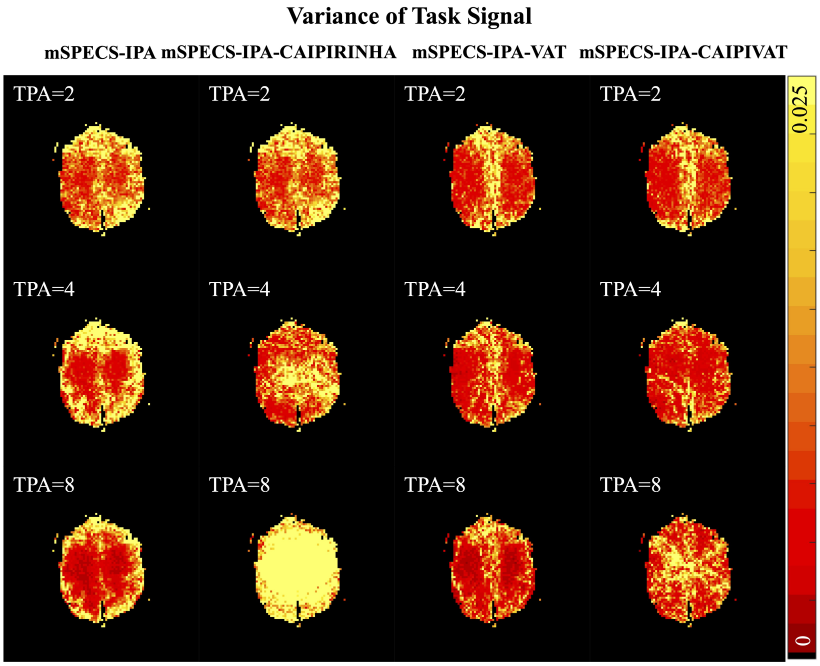

Figure A.24: The temporal variance of reconstructed image for slice 3 from mSPECS-IPA, mSPECS-IPA-CAIPIRINHA, mSPECS-IPA-VAT and mSPECS-IPA-CAIPIVAT model with different acceleration factor TPA=2, TPA=4, and TPA=8.

mSPECS-IPA-CAIPIRINHA model. The temporal variance in the mSPECS-IPA-CAIPIVAT model also increases, particularly in the central region of the brain, as the acceleration factor increases. However, in the two models without vertical image shift techniques, mSPECS-IPA and mSPECS-IPA-VAT, the temporal variance decreases. Moreover, in a comparison between these two models, the mSPECS-IPA-VAT model exhibits lower temporal variance in the left and right motor cortex regions of the brain as the acceleration factor increases.

References

[1] Barth, M., Breuer, F., Koopmans, P. J., Norris, D. G., and Poser, B. A. *Simultaneous multislice (SMS) imaging techniques.* Magn Reson Med. 75(1):63–81. https://doi.org/10.1002/mrm.25897.

[2] Breuer, F. A., Blaimer, M., Heidemann, R. M., Mueller, M. F., Griswold,

M. A., and Jakob, P. M. *Controlled aliasing in parallel imaging results in higher acceleration (CAIPIRINHA) for multi-slice imaging.* Magn Reson Med. 53(3):684–91. https://doi.org/10.1002/mrm.20401.

[3] Cho, Z. H., Kim, D. J., and Kim, Y. K. *Total inhomogeneity correction including chemical shifts and susceptibility by view angle tilting.* Medical physics. 15(1), 7-11. https://doi.org/10.1118/1.596162.

[4] Cauley, S. F., Polimeni, J. R., Bhat, H., Wald, L. L., and Setsompop, K. *Interslice leakage artifact reduction technique for simultaneous multislice acquisitions*, Magn Reson Med, 72(1), 93-102. https://doi.org/10.1002/mrm.24898

[5] Fletcher, D. W., Haselgrove, J. C., and Bolinger, L. *High-resolution imaging using Hadamard encoding.* Magnetic Resonance Imaging. 17(10), 1457-1468. https://doi.org/10.1016/S0730-725X(99)00098-3.

[6] Griswold, M. A., Jamob, P. M., Heidemann, R. M., Nikkka, M., Jellus, V., Wang, J., Kiefer, B., and Haase, A. *Generalized autocalibrating partially parallel acquisition (GRAPPA).* Magn Reson Med. 47:1202–1210. https://doi.org/10.1002/mrm.10171.

[7] Hyde, J. S., Jesmanowicz, A., Froncisz, W., Kneeland, J. B., Grist, T. M., and Campagna, N. F. *Parallel image acquisition from noninteracting local coils.* Journal of Magnetic Resonance. 70(3), 512-517. https://doi.org/10.1016/0022-2364(86)90146-0.

[8] Jungmann, P. M., Ganter, C., Schaeffeler, C. J., Bauer, J. S., Baum, T., Meier, R., Nittka, M., Pohlig, F., Rechl, H., von Eisenhart-Rothe, R., Rummeny, E. J., and Woertler, K. *View-Angle Tilting and Slice-Encoding Metal Artifact Correction for Artifact Reduction in MRI: Experimental Sequence Optimization for Orthopaedic Tumor Endoprostheses and Clinical Application.* PLoS One. 10(4):e0124922. https://doi.org/10.1371/journal.pone.0124922.

[9] Kociuba, C. M. *A Fourier description of covariance, and separation of simultaneously encoded slices with in-plane acceleration in fMRI.* Ph.D. Dissertation. Marquette University, Milwaukee, Wisconsin, USA. https://api.semanticscholar.org/CorpusID:114186307.

[10] Kim, M-O, Hong, T., and Kim, D-H. *Multislice CAIPIRINHA Using View Angle Tilting Technique (CAIPIVAT).* Tomography. 43-48. https://doi.org/10.18383/j.tom.2016.00109.

[11] Kim, M-O, Zho, S-Y, and Kim, D-H. *3D imaging using magnetic resonanace tomosynthesis (MRT) technique.* Med. Phys. 39(8): 4733-4741. https://doi.org/10.1118/1.4737111.

[12] Lin, F. H., Kwong, K. K., Belliveau, J. W., and Wald, L. L. *Parallel imaging reconstruction using automatic regularization.* Magnetic Resonance in Medicine. 51(3), 559-567. https://doi.org/10.1002/mrm.10718.

[13] Mansfield, P. *Multi-planar image formation using NMR spin echoes.* Journal of Physics C: Solid State Physics. 10(3): L55. https://dx.doi.org/10.1088/0022-3719/10/3/004.

[14] Ogawa, S., Lee, T. M., Kay, A. R., and Tank, D. W. *Brain magnetic resonance imaging with contrast dependent on blood oxygenation.* Proc Natl Acad Sci USA. 87(24):9868-721. https://doi.org/10.1073/pnas.87.24.9868.

[15] Pruessmann, K. P., Weiger, M., Scheidegger, M. B., and Boesiger, P. *SENSE: Sensitivity Encoding for Fast MRI.* Magn Reson Med. 42:952–962. https://doi.org/10.1002/(SICI)1522-2594(199911)42:5<952::AID-MRM16>3.0.CO;2-S

[16] Risk, B. B., Murden, R. J., Wu, J., Nebel, M. B., Venkataraman, A., Zhang, Z., and Qiu, D. *Which multiband factor should you choose for your resting-state fMRI study?* Neuroimage. 234:117965. https://doi.org/10.1016/j.neuroimage.2021.117965

[17] Rowe, D. B., Bruce, I. P., Nencka, A. S., Hyde, J. S., and Kociuba, M. C. *Separation of parallel encoded complex-valued slices (SPECS) from a signal complex-valued aliased coil image.* Magn Reson Imaging. 34(3):359-69. https://doi.org/10.1016/j.mri.2015.11.003

[18] Rowe, D. B. and Logan, B. R. *A complex way to compute fMRI activation.* Neuroimage. 23(3):1078-92. https://doi.org/10.1016/j.neuroimage.2004.06.042

[19] Rowe, D. B., Nencka, A. S., Jesmanowicz, A., and Hyde, J. S. *Separation of two simultaneously encoded slices with a single coil.* In Proc Intl Soc Magn Reson Med. Vol. 21, p. 0123.

[20] Redzian, R., Mansfield, P., and Doyle, M. *Real-time nuclear magnetic resonance clinical imaging in pediatrics.* Lancet. 322:1281-2. 10.1016/S0140-6736(83)91153-4.

[21] Sakitis, C. J., Brown, D. A., and Rowe, D. B. *A Bayesian complex-valued latent variable model applied to functional magnetic resonance imaging.* Journal of the Royal Statistical Society Series C: Applied Statistics. 74(1), 100-125. https://doi.org/10.1093/jrsssc/qlae046.

[22] Setsompop, K., Gagoski, B. A., Polimeni, J. R., Witzel, T., Wedeen, V. J., and Wald, L. L. *Blipped-controlled aliasing in parallel imaging (blipped-CAIPI) for simultaneous multi-slice EPI with reduced g-factor penalty.* Magn Reson Med. 67(5): 1210-1224. https://doi.org/10.1002/mrm.23097.

[23] Souza, S. P., Szumowskim, J., Dumoulin, C. L., Plewes, D. P., and Glover, G. *SIMA - simultaneous multislice acquisition of MR images by Hadamard-encoded excitation.* J Comput Assist Tomogr. 12:1026–1030.

[24] Stehling, M. K., Turner, R., and Mansfield, P. *Echo-planar imaging: magnetic resonance imaging in a fraction of a second.* Science. 254(5028), 43-50. DOI: 10.1126/science.1925560.

[25] Welvaert, M. and Rosseel, Y. *On the Definition of Signal-To-Noise Ratio and Contrast-To-Noise Ratio for fMRI Data.* J PloS ONE. 8(11): e77089. https://doi.org/10.1371/journal.pone.0077089.

[26] Xu, K., and Rowe, D. B. *A Bayesian CAIPIVAT approach with through-plane acceleration to enhance efficiency of simultaneously encoded slice acquisition in FMRI..* Magnetic Resonance Imaging. 110540. https://doi.org/10.1016/j.mri.2025.110540.